Three-Dimensional Turbulent Bottom Density Currents from a High-Order Nonhydrostatic Spectral Element Model

TAMAY M. ÖZGÖKMEN

Division of Meteorology and Physical Oceanography, Rosenstiel School of Marine and Atmospheric Science, University of Miami, Miami, Florida

PAUL F. FISCHER

Mathematics and Computer Science Division, Argonne National Laboratory, Argonne, Illinois

JINQIAO DUAN

Department of Applied Mathematics, Illinois Institute of Technology, Chicago, Illinois

TRAIAN ILIESCU

Department of Mathematics, Virginia Polytechnic Institute and State University, Blacksburg, Virginia

(Manuscript received 18 November 2003, in final form 5 April 2004)

ABSTRACT

Overflows are bottom gravity currents that supply dense water masses generated in high-latitude and marginal seas into the general circulation. Oceanic observations have revealed that mixing of overflows with ambient water masses takes place over small spatial and time scales. Studies with ocean general circulation models indicate that the strength of the thermohaline circulation is strongly sensitive to representation of overflows in these models. In light of these results, overflow-induced mixing emerges as one of the prominent oceanic processes. In this study, as a continuation of an effort to develop appropriate process models for overflows, nonhydrostatic 3D simulations of bottom gravity are carried out that would complement analysis of dedicated observations and large-scale ocean modeling. A parallel high-order spectral-element Navier–Stokes solver is used as the basis of the simulations. Numerical experiments are conducted in an idealized setting focusing on the startup phase of a dense water mass released at the top of a sloping wedge. Results from 3D experiments are compared with results from 2D experiments and laboratory experiments, based on propagation speed of the density front, growth rate of the characteristic head at the leading edge, turbulent overturning length scales, and entrainment parameters. Results from 3D experiments are found to be in general agreement with those from laboratory tank experiments. In 2D simulations, the propagation speed is approximately 20% slower than that of the 3D experiments and the head growth rate is 3 times as large, Thorpe scales are 1.3–1.5 times as large, and the entrainment parameter is up to 2 times as large as those in the 3D experiments. The differences between 2D and 3D simulations are entirely due to internal factors associated with the truncation of the Navier–Stokes equations for 2D approximation.

1. Introduction

A density current or gravity current is the flow of one fluid within another driven by the gravitational force acting on the density difference between the fluids. Density currents occur in a wide variety of circumstances. In the atmosphere, thunderstorm outflows and sea breeze fronts are gravity currents of cold dense air (Houze 1993). In rivers, turbidity currents whose density derives from suspended mud and silt can control deposition of sediment and have geological consequences. Other examples of phenomena induced by similar underlying physics are avalanches and ash clouds rushing down the mountains after volcanic eruptions (Simpson 1982).

Oceanic gravity currents are of particular importance because they are intimately related to the ocean's role in climate dynamics. The thermohaline circulation in the ocean is strongly influenced by dense-water formation that takes place mainly in polar seas by cooling (e.g., Dickson et al. 1990; Borenäs and Lundberg 1988) and in marginal seas by evaporation (e.g., the Mediterranean Sea; Baringer and Price 1997a). Such dense-water masses are released into the large-scale ocean

Corresponding author address: Tamay Özgökmen, RSMAS/MPO, University of Miami, 4600 Rickenbacker Causeway, Miami, FL 33149-1098.
E-mail: tozgokmen@rsmas.miami.edu

© 2004 American Meteorological Society

Unauthenticated | Downloaded 12/09/24 12:22 AM UTC

circulation in the form of overflows, which are bottom gravity currents. For instance, intense evaporation in the Mediterranean Sea produces salty water that sinks to the bottom and flows over the sill in the Strait of Gibraltar (Bryden and Kinder 1991) and forms a bottom density current that descends along the continental slope. If it did not mix with the Atlantic water, the Mediterranean water would be dense enough to sink to the bottom of the Atlantic Ocean. However, observations show that the Mediterranean salinity tongue spreads across the North Atlantic basin at middepths (Lozier et al. 1995), because it is diluted by entrainment of the overlying fresh Atlantic water (e.g., Price et al. 1993). Similar considerations apply to other overflows (e.g., Red Sea; Murray and Johns 1997; Denmark Strait; Girton et al. 2001). Studies by Jia (2000), Özgökmen et al. (2001), and Özgökmen and Crisciani (2001) indicate another aspect of overflows that has been appreciated only recently, namely, that the localized and persistent mixing between the Mediterranean overflow and the North Atlantic water also plays a role in the dynamics of the overlying upper-ocean currents. A systematic comparison of several realistic ocean circulation models for the North Atlantic circulation demonstrated that the large-scale thermohaline circulation is strongly sensitive to the representation of overflows in these models (Willebrand et al. 2001), which implies that the mixing of overflows with the ambient fluid may be an important factor in the long-term behavior of large-scale ocean circulation (with a potential impact on climate).

Ocean models of the type used for computing climate scenarios to the present day have inherent problems in modeling the large-scale effects of overflow plumes, mostly because these models cannot reproduce the product of the mixing processes where they enter into the ocean. Models either dilute the outflow water too strongly (e.g., in geopotential vertical coordinate models), thus destroying outflow signal, or they may not generate enough mixing without explicit parameterizations (e.g., in isopycnal coordinate models), resulting in the ''wrong'' product waters. An accurate representation of the mixing of overflows with ambient water masses is critical because it determines the properties of intermediate and deep water masses in the ocean. It is generally accepted from laboratory experiments (Simpson 1969) and observations (e.g., Baringer and Price 1997b) that mixing between density currents and the ambient fluid takes place primarily via vertical shear instability. Overflows have a small vertical scale, typically 100–300 m (Price and Yang 1998). The embedded overturns are smaller owing to limitations imposed by stable stratification. An explicit representation of mixing in overflows in numerical models requires not only a small vertical grid scale but also a horizontal grid scale small enough to capture the billows forming near the density interface. Oceanic observations indicate that the typical height-to-length ratio of Kelvin–Helmholtz billows is about 0.1 (e.g., Marmorino 1987). The typical resolution requirements for explicit resolution of billows are 10–30 m in the vertical direction and 100–300 m in the horizontal direction. As overflows propagate with speeds $O(1\ \mathrm{m\ s^{-1}})$, the time scale for the evolution of billows is $O(100\ \mathrm{s})$. Given the typical spatial resolution of 100 km (5–20 km) and time steps O(hour) in climate (large-scale ocean) models, spatial and time scales to resolve overflows are computationally prohibitive at the present time.

In addition to model resolution and vertical coordinate system, another issue is that most ocean models are based on hydrostatic primitive equations. According to the hydrostatic approximation, the primary dynamical balance in the vertical momentum equation is between the pressure gradient and gravitational buoyancy acceleration terms. Therefore, vertical acceleration terms are omitted, and vertical mixing processes important in the dynamics of overflows are misrepresented.

Because of the importance of overflows, there has been significant effort to address these dynamical and modeling issues. Considerable progress has been achieved in improving the downslope flow of overflows in geopotential vertical coordinate models (e.g., Beckmann and Döscher 1997; Winton et al. 1998; Killworth and Edwards 1999; Nakano and Suginohara 2002). Also, turbulence closures have been tried in terrain-following models (e.g., Jungclaus and Mellor 2000) and a mixing parameterization based on laboratory experiments (Turner 1986) has been implemented in isopycnal models with encouraging results (Hallberg 2000; Papadakis et al. 2003).

Despite the recent progress, a critical issue that remains to be addressed is the details of mixing and entrainment in bottom density currents. The present level of our systematic understanding of such mixing is derived from laboratory tank experiments (Ellison and Turner 1959; Simpson 1969, 1982, 1987; Britter and Linden 1980; Turner 1986; Hallworth et al. 1996; Monaghan et al. 1999; Baines 2001). However, when configured for the small slopes of observed overflows [$O(1°)$], the dense source fluid cannot accelerate enough within the bounds of typical laboratory tanks [$O(1\ \mathrm{m})$] to produce turbulent behavior. For turbulence to occur, laboratory experiments are configured with slopes greater than 10°. It is also difficult to maintain a complex ambient stratification in these tanks.

Given recent advances in numerical techniques and computer power, numerical modeling provides an alternative avenue to investigate these processes. Nonhydrostatic, high-resolution, two-dimensional simulations of bottom gravity currents have been conducted by Özgökmen and Chassignet (2002) that capture explicitly the major features of these currents seen in laboratory experiments, such as the presence of a head in the leading edge and Kelvin–Helmholtz vortices in the trailing fluid. Subsequently, this model was used to simulate the part of the Red Sea outflow in a submarine canyon, which naturally restricts motion in the lateral

Unauthenticated | Downloaded 12/09/24 12:22 AM UTC

direction such that the use of a 2D model provides a reasonable approximation to the dynamics. It was shown (Özgökmen et al. 2003) that this model adequately captures the general characteristics of mixing in the Red Sea overflow within the limitations of a 2D model, such as lack of edge effects or intrusions from channel walls associated with the spanwise structure. The 2D numerical model employed in these studies provides simplicity and computational efficiency. However, by allowing only the spanwise component of vorticity, a 2D model imposes an obvious limitation on the equations of motion, hence potentially on the mixing of bottom gravity currents with ambient fluid. Therefore, the logical next step is to conduct 3D numerical simulations of bottom gravity currents.

In this study, the primary objective is to determine differences between 2D and 3D simulations of bottom gravity currents. To this end, the experimental setup in Özgökmen and Chassignet (2002) is adopted, in which the initial evolution of a dense water mass released at the top of a sloping wedge at a constant angle is explored. A high-order spectral element Navier-Stokes solver (Fischer 1997; Fischer et al. 2000; Tufo and Fischer 1999; Fischer and Mullen 2001) is used as the basis for our simulations. First, a 2D turbulent simulation is conducted. Then, the domain is extended in the spanwise direction, and equivalent 3D simulations are conducted. To our knowledge, the present numerical simulations are the first to explicitly model 3D shear instability in bottom gravity currents propagating over a sloping topography. The differences between 2D and 3D simulations are quantified by comparing the evolution of characteristic features such as the head of the dense plume, Kelvin–Helmholtz waves, speeds of descent, turbulent overturning length scales, and entrainment parameters.

The paper is organized as follows. In section 2, the method is outlined and the numerical model introduced. The experimental setup and parameters are outlined in section 3. Qualitative and quantitative comparisons of 2D and 3D simulations are presented in section 4. Last, the principal results and future directions are summarized in section 5.

2. Approach

a. Model requirements

Bottom density currents have been traditionally investigated by using so-called stream-tube models. These models have been useful in examining the path and bulk properties of the Denmark Strait overflow (e.g., Smith 1975), Weddell Sea overflow (Killworth 1977), the Mediterranean overflow (Baringer and Price 1997b), and initial studies of the Red Sea overflow (Bower et al. 2000). Various simplifications are required in these models, such as steady state, motionless ambient fluid, simple topography, and mixing parameterization based on laboratory experiments. In recent years, a number of studies have employed more complex models. Jungclaus and Backhaus (1994) used a primitive equation, 2D (x, y) shallow-water model with reduced gravity approximation in the vertical direction. They conducted idealized experiments to investigate the effects of bottom friction and topography, and they also applied their model to the Denmark Strait overflow. Özsoy et al. (2001) used the same model in an analysis of the overflow from the Bosphorus into the Black Sea and concluded that the slope and finescale features of the bottom topography are crucial elements in determining plume behavior. Gawarkiewicz and Chapman (1995) used a 3D hydrostatic model to explore the development of a plume with negative buoyancy. They found that the leading edge of the plume forms eddies in the horizontal plane and concluded that instabilities and eddy fluxes are important mechanisms for the transport of dense waters, in contrast to the quasi-steady behavior implied from streamtube models. This conclusion is also supported by numerical studies by Jiang and Garwood (1995, 1996), who used a different 3D, hydrostatic, sigma-coordinate model. Jiang and Garwood (1998) concluded that topographic variations induce significant changes in the mixing and entrainment between density currents and ambient fluid. Sigma- and isopycnic-coordinate ocean general circulation models have been used to simulate the Mediterranean overflow (Jungclaus and Mellor 2000; Papadakis et al. 2003) employing various mixing parameterizations (Mellor and Yamada 1982; Hallberg 2000). These modeling studies have led to a significant understanding of bottom density currents in the ocean. However, none of the studies explicitly resolve and capture shear instabilities at the density interface between the gravity current and ambient fluid, which lead to mixing and entrainment. This is partly because of inadequate resolution to capture the scales of such motion and partly because of hydrostatic dynamics.

Following nonhydrostatic, high-resolution 2D simulations of bottom gravity currents in idealized (Özgökmen and Chassignet 2002) and realistic (Özgökmen et al. 2003) setttings, the logical next step is 3D nonhydrostatic modeling of bottom gravity currents. The numerical model used in previous studies is based on strictly 2D (streamfunction–vorticity) formulation and relatively low-order (second-order finite difference) numerics, whereas the high computational cost of 3D simulations necessitates high-order models to minimize the number of grid points, and techniques to obtain good scalability on parallel computers. In this study, a state-of-the-art spectral element model is used, the details of which are described in the following.

b. Equations of motion

The momentum and continuity equations subject to the Boussinesq approximation can be written as follows:

Unauthenticated | Downloaded 12/09/24 12:22 AM UTC

$$\frac{D\mathbf{u}}{Dt} = -\frac{1}{\rho_0}\nabla p + \nu_h\nabla_r^2\mathbf{u} - g\frac{\rho'}{\rho_0}\hat{\mathbf{z}} \quad \text{and} \tag{1}$$

$$\nabla\cdot\mathbf{u} = 0, \tag{2}$$

where $\mathbf{u} = (u, v, w)$ is the velocity vector field, p is the pressure, $g = 9.81\ \text{m}^2\ \text{s}^{-1}$ is the gravitational acceleration, ν_h is the viscosity in the horizontal direction, and $\hat{\mathbf{z}}$ is the unit normal vector in the vertical direction. The material (total) derivative is

$$\frac{D}{Dt} = \frac{\partial}{\partial t} + \mathbf{u}\cdot\nabla, \tag{3}$$

and the anisotropic diffusivity is

$$\nabla_r^2 = \frac{\partial^2}{\partial x^2} + \frac{\partial^2}{\partial y^2} + r\frac{\partial^2}{\partial z^2}, \tag{4}$$

where $r = \nu_v/\nu_h$ is the ratio of vertical to horizontal diffusivities. A linear equation of state

$$\rho' = \rho_0\beta S \tag{5}$$

is used, where ρ_0 is the background water density, $\beta = 7\times10^{-4}\ \text{psu}^{-1}$ is the salinity contraction coefficient, and S is the salinity deviation from a background value. The equation for salinity transport is

$$\frac{DS}{Dt} = K_h\nabla_r^2 S, \tag{6}$$

where we assume that the vertical and horizontal diffusivities also satisfy $r = K_v/K_h$.

Nondimensionalizing (1)–(6) by

$$(x,y,z) = H(x^*,y^*,z^*), \qquad (u,v,w) = \frac{\nu_h}{H}(u^*,v^*,w^*),$$

$$t = \frac{H^2}{\nu_h}t^*, \qquad p = \frac{\rho_0\nu_h^2}{H^2}p^*, \quad \text{and} \quad S = \Delta S S^*, \tag{7}$$

where H is the domain depth and ΔS is the amplitude of the salinity range in the system, and dropping the asterisk, we obtain for the equations of motion in 3D

$$\frac{D\mathbf{u}}{Dt} = -\nabla p + \nabla_r^2\mathbf{u} - \text{Ra}S\hat{\mathbf{z}}, \tag{8}$$

$$\nabla\cdot\mathbf{u} = 0, \quad \text{and} \tag{9}$$

$$\frac{DS}{Dt} = \text{Pr}^{-1}\nabla_r^2 S, \tag{10}$$

where $\text{Ra} = (g\beta\Delta S H^3)/\nu_h^2$ is the Rayleigh number, the ratio of the strengths of buoyancy and viscous forces, and $\text{Pr} = \nu_h/K_h$ is the Prandtl number, the ratio of viscous and saline diffusion. The two-dimensional variant of (8)–(10) is obtained by enforcing $v = 0$ and disallowing variations in y.

c. Numerical model

The time advancement of (8)–(10) is based on second-order semi-implicit operator-splitting methods developed by Maday et al. (1990) and described in Fischer (1997). The hydrodynamics (8)–(9) are advanced first, with explicit treatment of the Boussinesq forcing term, $\text{Ra}S\hat{\mathbf{z}}$, followed by the update of the salinity transport. As suggested by Pironneau (1982), the material derivatives are approximated by second-order finite differences along the characteristics,

$$\left.\frac{D\phi}{Dt}\right|_{t^n} \approx \frac{3\phi^n - 4\tilde{\phi}^{n-1} + \tilde{\phi}^{n-2}}{2\Delta t}, \tag{11}$$

where ϕ^n represents the transported scalar field (u, v, w, or S) at time level t^n and Δt is the timestep size. The quantities $\tilde{\phi}^{n-q}$ represent the value of ϕ at the foot of the characteristics associated with time level t^{n-q}. Following Maday et al. (1990), these values are computed by solving the following initial boundary value problems on $[t^{n-q}, t^n]$:

$$\frac{\partial\tilde{\phi}}{\partial t} + \mathbf{u}\cdot\nabla\tilde{\phi} = 0 \quad \text{and}$$

$$\tilde{\phi}(\mathbf{x}, t^{n-q}) = \phi(\mathbf{x}, t^{n-q}). \tag{12}$$

Equation (12) is solved using an explicit fourth-order Runge–Kutta scheme with step size $\Delta s \le \Delta t$, which satisfies an appropriate Courant condition. The values of $\mathbf{u}$ in (12) are interpolated/extrapolated from the previous velocity fields, $(\mathbf{u}^{n-q}, \ldots, \mathbf{u}^{n-1})$.

Inserting the approximation (11) into (8)–(10) and rearranging with the precomputed values of $\tilde{\mathbf{u}}^{n-q}$ and $\tilde{S}^{n-q}$ leads to a linear subproblem to be solved at each time step:

$$\left(\frac{3}{2\Delta t} - \nabla^2\right)\mathbf{u}^n + \nabla p^n = \frac{1}{2\Delta t}(4\tilde{\mathbf{u}}^{n-1} - \tilde{\mathbf{u}}^{n-2}) - \text{Ra}\overline{S}^n\hat{\mathbf{z}}, \tag{13}$$

$$\nabla\cdot\mathbf{u}^n = 0, \quad \text{and} \tag{14}$$

$$\left(\frac{3}{2\Delta t} - \nabla^2\right)S^n = \frac{1}{2\Delta t}(4\tilde{S}^{n-1} - \tilde{S}^{n-2}). \tag{15}$$

The value of $\overline{S}^n$ is an extrapolated second-order approximation to S^n, which imposes a stability constraint on Δt. This constraint, however, is generally less severe than the standard Courant stability criterion, which is effectively eliminated by the characteristics-based approach outlined above. The Courant number is typically ≈ 1, and the overall scheme is second-order accurate in time.

Spatial discretization of (13)–(15) is based upon the spectral element method (SEM; Patera 1984; Maday and Patera 1989; Fischer 1997), which combines the high-order accuracy of spectral methods with the geometric flexibility of traditional finite-element methods. For conciseness, we focus on the Stokes problem (13)–(14) and assume that the velocity satisfies homogeneous Dirichlet conditions on the boundary $\partial\Omega$. The salinity transport equation is discretized in an analogous way.

Unauthenticated | Downloaded 12/09/24 12:22 AM UTC

As with the finite-element method, the SEM is based on a Galerkin formulation in which (13)–(14) are formally multiplied by a set of test functions $(\mathbf{v}, q) \in (X^N, Y^N)$ and integrated over the computational domain Ω, where X^N, and Y^N are finite-dimensional function spaces to be defined. The solution is determined by requiring $(\mathbf{u}, p) \in (X^N, Y^N)$ to satisfy

$$\frac{3}{2\Delta t}(\mathbf{v}, \mathbf{u}) + (\nabla \mathbf{v}, \nabla \mathbf{u}) - (\nabla \cdot \mathbf{v}, p^n) = \frac{1}{2\Delta t}(\mathbf{v}, \mathbf{f}) \quad (16)$$

and

$$(q, \nabla \cdot \mathbf{u}^n) = 0, \quad (17)$$

for all $(\mathbf{v}, q) \in (X^N, Y^N)$. Here, $\mathbf{f}$ is assumed to be the interpolant of the the right-hand side of (13), and the scalar and vector inner products on the domain Ω are

$$(f, g) = \int_\Omega fg \, d\mathbf{x} \quad \text{and} \quad (\mathbf{f}, \mathbf{g}) = \int_\Omega \mathbf{f} \cdot \mathbf{g} \, d\mathbf{x},$$

respectively.

The spectral element discretization is determined by the choice of respective velocity and pressure spaces, X^N and Y^N. In the SEM, the computational domain $\Omega = U_k \Omega^k$ is subdivided into hexahedral elements Ω^k, $k = 1, \ldots, K$, each of which is mapped to the reference domain $\hat{\Omega} = [-1, 1]^3$. Functions in X^N are required to be continuous and are expressed as tensor-product Lagrange polynomials of degree N in the reference domain. For example, a single component of the velocity field in two dimensions would have the form

$$u(\mathbf{x})|_{\Omega^k} = \sum_{i=0}^{N} \sum_{j=0}^{N} u_{ij}^k \pi_i(\xi) \pi_j(\eta), \quad (18)$$

where u_{ij}^k are the set of basis coefficients; π_i, $i = 0, \ldots, N$, are the Nth-order Lagrange interpolants satisfying $\pi_i(\xi_p) = \delta_{ip}$; $\xi_p \in [-1, 1]$, $p = 0, \ldots, N$, are the Gauss–Lobatto–Legendre quadrature points; and δ_{ip} is the Kronecker delta function. Implicit in the representation (18) is an isoparametric mapping from the computational domain, $(\xi, \eta) \in \hat{\Omega}$, to the element subdomain, $\mathbf{x} = (x, y) \in \Omega^e$. Accurate derivatives are computed by differentiating the high-order basis functions in the reference domain and using the chain rule to map to the physical domain. Continuity of functions in X^N is enforced by constraining coefficients at coincident nodal points to be equal. Similarly, homogeneous Dirichlet conditions are enforced by constraining coefficients at nodal points on the boundary to be zero. Further details may be found in (Deville et al. 2002).

The pressure space, Y^N, is similar to the velocity space, save that interelement continuity is not enforced and that pressure boundary conditions are not applied. In addition, in order to be compatible with the velocity, the pressure is a tensor-product polynomial of degree $N - 2$ (Maday and Patera 1989). A typical representation in 2D is

$$p(\mathbf{x})|_{\Omega^k} = \sum_{i=1}^{N-1} \sum_{j=1}^{N-1} p_{ij}^k \tilde{\pi}_i(\xi) \tilde{\pi}_j(\eta), \quad (19)$$

where p_{ij}^k are the set of unknown basis coefficients; $\tilde{\pi}_i$, $i = 1, \ldots, N - 1$, are the Lagrange polynomial interpolants of order $N - 2$ satisfying $\tilde{\pi}_i(\tilde{\xi}_p) = \delta_{ip}$; and $\tilde{\xi}_p \in (-1, 1)$, $p = 1, \ldots, N - 1$, are the quadrature points associated with the $(N - 1)$-point Gauss–Legendre quadrature formula. Maday and Patera (1989) establish that this velocity–pressure pairing results in a stable discretization with an error that scales as α^N, $\alpha < 1$, that is, decays exponentially fast. Thus, although the pressure is formally discontinuous, it converges exponentially fast to a continuous solution.

By substituting the bases of the form (18) for the components of $\mathbf{v}$ and $\mathbf{u}$ and expressions similar to (19) for q and p into (16)–(17), coupled with the continuity constraint, one arrives at a large sparse linear system for the velocity and pressure. This system is solved iteratively and so in practice is never explicitly formed. One simply evaluates the *action* of the system on the corresponding iteration vector. The system is further simplified in two ways. First, all integration is carried out using pointwise quadrature. Inner products involving p or q are evaluated using $(N - 1)$-point Gauss–Legendre quadrature based on the nodal points $\tilde{\xi}_i$. All other inner products (including those for the salinity transport equation) are evaluated using $(N + 1)$-point Gauss–Lobatto–Legendre quadrature based on the nodal points ξ_i. The use of pointwise quadrature reduces the overall operation count and makes the SEM qualitatively similar to pseudospectral methods, in which nonlinear or nonconstant-coefficient terms are evaluated pointwise in physical space. Second, the viscous-pressure terms are decoupled into separate subproblems through the introduction of an additional time splitting. The usual ambiguities of appropriate boundary conditions for the pressure, however, are avoided because the splitting is performed on the *discrete* system, for which proper boundary conditions are already established. Details of the splitting can be found in Fischer (1997).

The time splitting leads to four independent elliptic solves. For each velocity component, there is a well-conditioned system that is readily solved by diagonally preconditioned conjugate gradient iteration. In addition, there is a divergence-free-projection step, which effectively requires a Poisson solve for the pressure, which is also solved using conjugate gradients. This latter system is preconditioned using a domain decomposition strategy based on the additive overlapping Schwarz method of Dryja and Widlund (1987). Details of the solution strategy are given in Fischer (1997) and Fischer et al. (2000).

We remark that the use of pointwise quadrature for the advective terms in (12) can lead to aliasing errors and consequent stability problems, as noted by Orszag (1972), and Kirby and Karniadakis (2003). While the advective term nominally only transports energy, rather

Unauthenticated | Downloaded 12/09/24 12:22 AM UTC

than creating or destroying it, the numerical discretization may not make such a balance. Galerkin formulations, however, will be energy conservative, provided that exact quadrature is used. The use of approximate quadrature in the SEM does not adversely affect the *accuracy* because the quadrature error is of the same order as the approximation error. It can, however, influence *stability*. That is, some of the eigenvalues associated with advective transport, which are nominally purely imaginary (energy is neither created nor destroyed), can take on nontrivial real components if pointwise quadrature is used. The potential ill effects of this shift can be eliminated by integrating with more points, so that the quadrature is exact, or by applying a small amount of high-wavenumber dissipation to the system through the use of a filter. We have chosen the latter course, following the procedure outlined in Fischer and Mullen (2001), where it was shown that the proposed filtering procedure does not compromise spectral accuracy.

3. Model configuration and parameters

The model domain is configured with a horizontal length of $L_x = 10$ km. The depth of the water column ranges from 400 m at $x = 0$ to $H = 1000$ m at $x = 10$ km over a constant slope. Hence the slope angle is $\theta = 3.5°$, which is within the general range of oceanic overflows, such as the Red Sea overflow entering the Tadjura Rift (e.g., Özgökmen et al. 2003). In the 3D case, the domain is extended by $L_y = 2$ km in the spanwise direction (Fig. 1a).

The boundary conditions at the bottom are no-slip and no-normal flow for the velocity components and no-normal flux, $\partial S/\partial \mathbf{n} = 0$, with $\mathbf{n}$ being the normal direction to the boundary, for salinity (Fig. 1a). At the top boundary, free-slip and rigid-lid boundary conditions are used. The model is entirely driven by the velocity and salinity forcing profiles at the inlet boundary at $x = 0$. The velocity distribution at the inlet (Fig. 1b) matches no-slip at the bottom and free-slip at the top using fourth-order polynomials such that the depth integrated mass flux across this boundary is zero. The model is initialized by using a salinity distribution of the form

$$S(x, y, z, t = 0) = \frac{1}{2}\exp\left\{-\left[\frac{x}{1 + a\sin(\pi y)}\right]^{20}\right\} \times \left[1 - \cos\left(\pi\frac{1 - z}{0.4}\right)\right].$$

The sinusoidal perturbation in the y direction facilitates transition to 3D flow in the 3D experiments. The transition from dense water at the bottom to overlying light water is consistent with the flow reversal for the velocity boundary condition (Fig. 1b). Imposing a steady inlet velocity profile independent of the interior dynamics of the density current would lead to either a recirculating flow at the inlet in the case of overestimation or a thinning down of the density current as it flows downslope because of an inadequate rate of supply. In order to avoid this, the amplitude of inflow velocity profile was made time dependent and scaled with the propagation speed of the gravity current, which is zero at $t = 0$ and reaches a constant value shortly after release (as shown below). Outflow boundary conditions of the type $\partial \mathbf{u}/\partial x = \partial S/\partial x = 0$ are used at the exit boundary at $x = L_x$. Because the interior is initialized with homogenous, light ($S = 0$) water, the density front propagation is the fastest signal in the system (as opposed to a stratified interior, which may permit faster internal waves). By terminating the integrations before the nose of density current reaches this boundary, the potential complications involving the outflow boundary are avoided, albeit with the limitation of focusing only on the ''start up'' phase of plumes rather than those in a statistically steady state. Last, periodic boundary conditions are applied at the lateral boundary for 3D simulations.

The main parameters of the system are the Rayleigh number Ra, the Prandtl number Pr, and the diffusivity ratio r. The Prandtl numbers are well known at the microscale (Pr $\approx$ 7 for temperature and Pr $\approx$ 700 for salinity), but these values are not well defined for larger scales. Here, it is assumed that the impact of turbulent motion is much higher than that of molecular diffusivities on the effective subgrid-scale diffusion, such that there is no difference between turbulent viscosity and diffusivity, and Pr = 1. This assumption is supported by laboratory data from Webster (1964). Owing to the high aspect ratio of ocean basins [$O(10^6$ m) wide but $O(10^3$ m) deep], it is generally assumed that diapycnal diffusivity is very small ($K \approx 10^{-5}$ m^2 s^{-1} and r $\ll$ 1). This observation clearly applies to large-scale flows because the ocean maintains a characteristic stratification over long time scales. However, this observation no longer applies near boundaries, regions of forcing, localized dissipation, and internal waves, all of which characterize overflows. Here, the vertical mixing ratio is chosen such that the horizontal and vertical diffusion terms in the momentum equations are approximately equal, that is, $r \approx O(H^2/L_x^2) \approx 10^{-2}$, and specifically $r = 2 \times 10^{-2}$ in this study. Last, because Ra represents the range of turbulent scales, the highest Ra permitted by the numerical resolution is used, and Ra $= 5 \times 10^6$ in the experiments presented below. In terms of dimensional quantities, this corresponds to $\Delta S = 1$ psu and $\nu_h \approx 1$ m^2 s^{-1}.

An important factor in the dynamics of oceanic overflows is rotation. The scale at which the Coriolis force becomes comparable to buoyancy force is a complex function of the slope angle, stratification, and friction (e.g., Griffiths 1986). A simple spatial scale for rotational effects to become important is given by the radius of deformation $\sqrt{g'h}/f$, which is approximately 17 km at midlatitudes with the experimental parameters, as

Unauthenticated | Downloaded 12/09/24 12:22 AM UTC

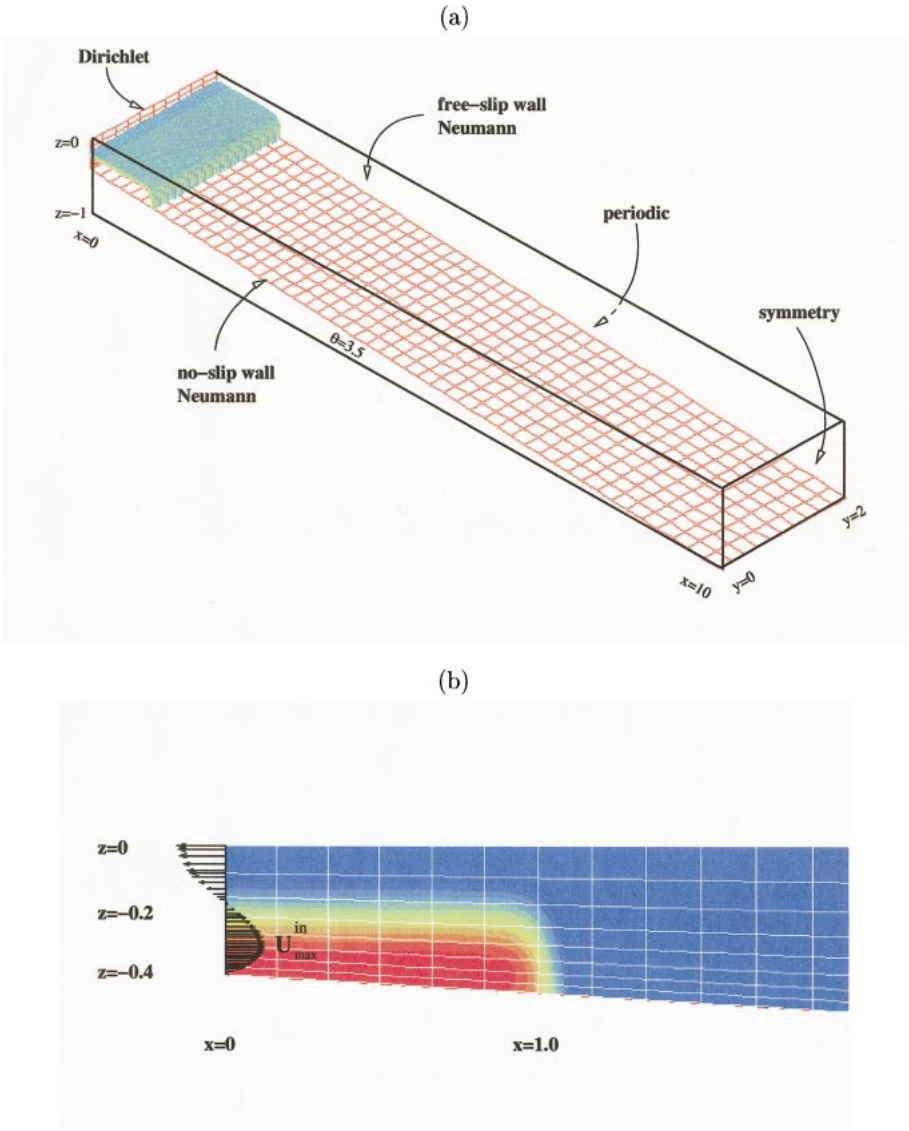

FIG. 1. (a) Schematic depiction of the domain geometry and boundary conditions (length scale is in kilometers). (b) Velocity profile at the forcing boundary and the initial distribution of salinity. Distribution of elements is depicted in the background. Color scale is in Fig. 2.

compared with $L_x = 10$ km. The rotation time scale is $f^{-1} \approx 15\,000$ s while, as shown below, the gravity currents cross the domain is $\approx$10 000 s. Hence, the results presented here apply to the phase before the impact of rotation starts influencing the flow patterns. Therefore, rotation is neglected here as a first-order approximation; it will be the focus of a future investigation. Last, neglect of rotation allows us to compare results from numerical experiments with those from laboratory experiments, the great majority of which have been conducted in the absence of rotation.

The spectral element method offers a dual approach to convergence: algebraic via elemental grid refinement, and exponential via increase in the order of intra-element interpolation. We therefore chose to use a minimum number of elements so that the shape of the domain geometry is adequately captured and the element size is adjusted to better capture the bottom boundary layer. Once the element distribution satisfies these criteria, we increase the spectral truncation degree for the convergence of the technique. In general, the numerical solution of the physical problem of interest benefits from two well-known features of spectral element models: the lack of numerical dissipation and excellent phase properties.

The 2D mesh has $K = 400$ elements (50×8 in the x and z directions), and the 3D mesh has $K = 4000$ elements ($50 \times 8 \times 10$ in the x, z, and y directions). The elements have a smaller vertical scale toward the bottom boundary and follow topography (Fig. 1b).

Unauthenticated | Downloaded 12/09/24 12:22 AM UTC

TABLE 1. Parameters of the numerical simulations.

Domain size (L_x, $L_z = H$, L_y)	In 2D (10^4 m, 10^3 m); in 3D (10^4 m, 10^3 m, 2×10^3 m)
Slope angle	$\theta = 3.5°$
Rayleigh No.	$\mathrm{Ra} = 5 \times 10^6$
Prandtl No.	$\mathrm{Pr} = 1$
Diffusivity ratio	$r = 2 \times 10^{-2}$
Viscosities	$\nu_h = 1.17\ \mathrm{m^2\ s^{-1}}$ and $\nu_v = 2.34 \times 10^{-2}\ \mathrm{m^2\ s^{-1}}$
Diffusivities	$K_h = 1.17\ \mathrm{m^2\ s^{-1}}$ and $K_v = 2.34 \times 10^{-2}\ \mathrm{m^2\ s^{-1}}$
Salinity range	$\Delta S = 1.0$ psu
No. of elements (x, z, y)	In 2D (50, 8); in 3D (50, 8, 10)
Polynomial degreee	$N = 10$
No. of grid points	In 2D 4×10^4; in 3D 4×10^6
Time step	$\Delta t = 0.85$ s

Therefore, the discretization is free from chronic problems encountered in Cartesian-coordinate models (e.g., Winton et al. 1998). The results presented in this paper are obtained by using spectral truncation with a polynomial degree of $N = 10$, which corresponds to 4×10^4 grid points for the 2D case and 4×10^6 grid points in the 3D case. With a time step of $\Delta t = 10^{-6}$ (0.85 s), the Courant number remains $C < 1$ throughout the simulations. (Experiments repeated with $N = 6$ show no significant difference from those with $N = 10$.) The model parameters are summarized in Table 1.

The experiments are conducted on a Beowulf Linux cluster consisting of 17 nodes with 1 GByte $\mathrm{s^{-1}}$ Ethernet connectivity. Each node has dual Athlon 1.7-GHz processors with 1024 MByte of memory. Two-dimensional simulations are conducted on 16 processors and take approximately 2 h (simulated to a real-time ratio of $\approx$2), whereas 3D simulations take approximately 9 days on 32 processors (simulated to a real-time ratio of $\approx$1/60).

4. Results

The experimental strategy is as follows. The 2D experiment, designated as EXP-2D, is compared with 3D experiments, EXP-3Da and EXP-3Db, which differ only in the spanwise initialization of the density current. We compare the experiments first qualitatively and then quantitatively using downslope propagation speeds, growth rates of the head, turbulent overturning length scales, and entrainment parameters.

a. Description of the experiments

The evolution of the salinity distribution in EXP-2D is shown in Fig. 2a. The system is initialized as described in section 3 and starts from rest. The initial development of the system is that of the so-called lock-exchange flow (e.g., Keulegan 1958; Simpson 1987), in which the lighter fluid remains on top and the denser overflow propagates downslope. The dense gravity current quickly develops a characteristic ''head'' at the leading edge of the current (Fig. 2b). The head is one-half of a dipolar vortex, which is a generic flow pattern that tends to form in two-dimensional systems by self-organization of the flow (e.g., Flierl et al. 1981; Nielsen and Rasmussen 1996) and that corresponds to the most probable equilibrium state maximizing entropy (Smith 1991). Initially, the gravity current is stable, but by the time the current travels one-half of the domain length, the head becomes unstable, exhibiting breaking waves and intense mixing (Fig. 2c). The head grows and is diluted as the gravity current travels further down the slope, the result of entrainment of fresh ambient fluid. The trailing current, the ''tail,'' initially displays only some patterns of waves, but later (Fig. 2c) the instability near the top of the tail leads to a rolling up of the density interface in lumped vortices separated by a characteristic length scale. This behavior is clearly indicative of the Kelvin–Helmholtz instability, in which waves made up of fluid from the current entrap the ambient fluid (e.g., Corcos and Sherman 1984). Initially, Kelvin–Helmholtz rolls also remain quite stable and grow in size by entrainment of ambient fluid and vortex pairing (e.g., Klaassen and Peltier 1989). Eventually, the system becomes quite complex, exhibiting shedding of dense blobs and localized features resembling hydraulic jumps (Figs. 2d,e). These features were not observed in previous 2D simulations by Özgökmen and Chassignet (2002), which were conducted at lower Ra ($\approx 5 \times 10^4$–30×10^4, in our units) because of the lower order and convergence of the finite-difference method with respect to that of the spectral-element method. The integration is terminated once the density front reaches $x \approx L_x$ (Fig. 2e).

The 3D experiments are conducted by simply extending the domain in the spanwise direction by $L_y = 2$ km and applying periodicity at the lateral boundaries. A sinusiodal perturbation is imposed on the density current initialization in the spanwise direction (Fig. 3a, corresponding to $a = 0.1$) to accelerate the transition to 3D flow. Other options to facilitate 3D breakdown include 1) addition of random perturbations to the equations of motion and 2) introduction of y-dependent forcing as velocity or salinity boundary conditions. However, using option 1 could potentially degrade the high accuracy of the model numerics, and option 2 could act in a way that it is no longer valid to compare 2D and 3D cases. Here, EXP-3Da simulation remains equivalent

Unauthenticated | Downloaded 12/09/24 12:22 AM UTC

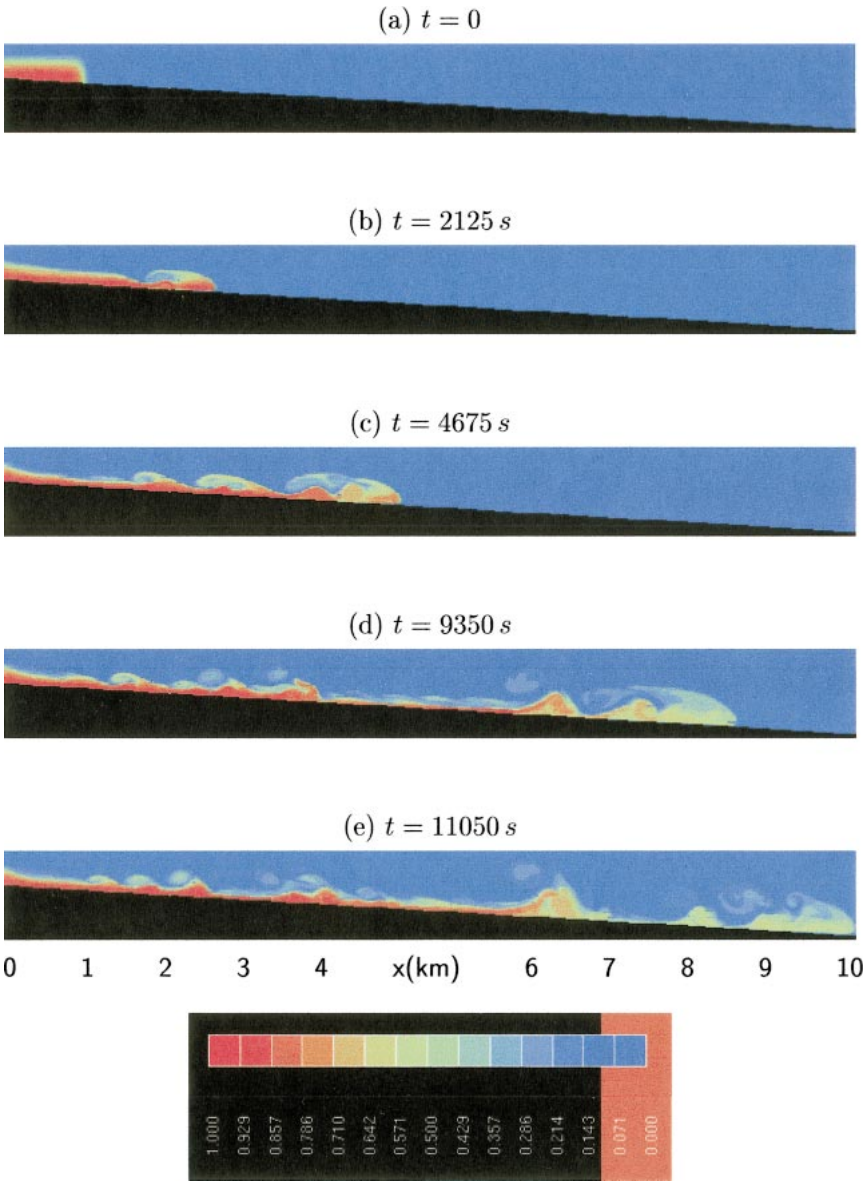

FIG. 2. Salinity distribution in EXP-2D at (a) $t = 0$, (b) $t = 2125$ s (≈0.6 h), (c) $t = 4675$ s (≈1.3 h), (d) $t = 9350$ s (≈2.6 h), and (e) $t = 11050$ s (≈3.1 h).

to EXP-2D in the spanwise-integrated sense, in terms of parameters, forcing, and initialization.

As the gravity current starts from rest (Fig. 3a), the initial perturbations actually decay such that the current becomes nearly 2D at the beginning (Fig. 3b). As the system gains enough inertia, 3D perturbations amplify (Fig. 3c) and make significant changes in both the head and trailing fluid. The flow along the leading edge of the current is composed of a complex pattern of so-called lobes and clefts that are highly unsteady (Figs. 3c,d) and well-known features from laboratory experiments tracing back to the work of Simpson (1972). It was conjectured (e.g., Simpson 1987) that a gravitational rise of the thin layer of light fluid that the gravity current overruns is responsible for the breakdown of the flow at the leading edge. Recently, Härtel et al. (2000) put forth that instability associated with the unstable stratification prevailing at the leading edge between the nose and stagnation point of the front could also account for this behavior. In the trailing fluid, the initial instabilities appear to be 2D Kelvin–Helmholtz rolls that span the entire width of the domain (Fig. 3c). These rolls gradually exhibit transition to 3D (Fig. 3d). The development of spanwise instabilities in Kelvin–Helmholtz rolls was investigated by Klaassen and Peltier (1991), who classified them into two categories. First

Unauthenticated | Downloaded 12/09/24 12:22 AM UTC

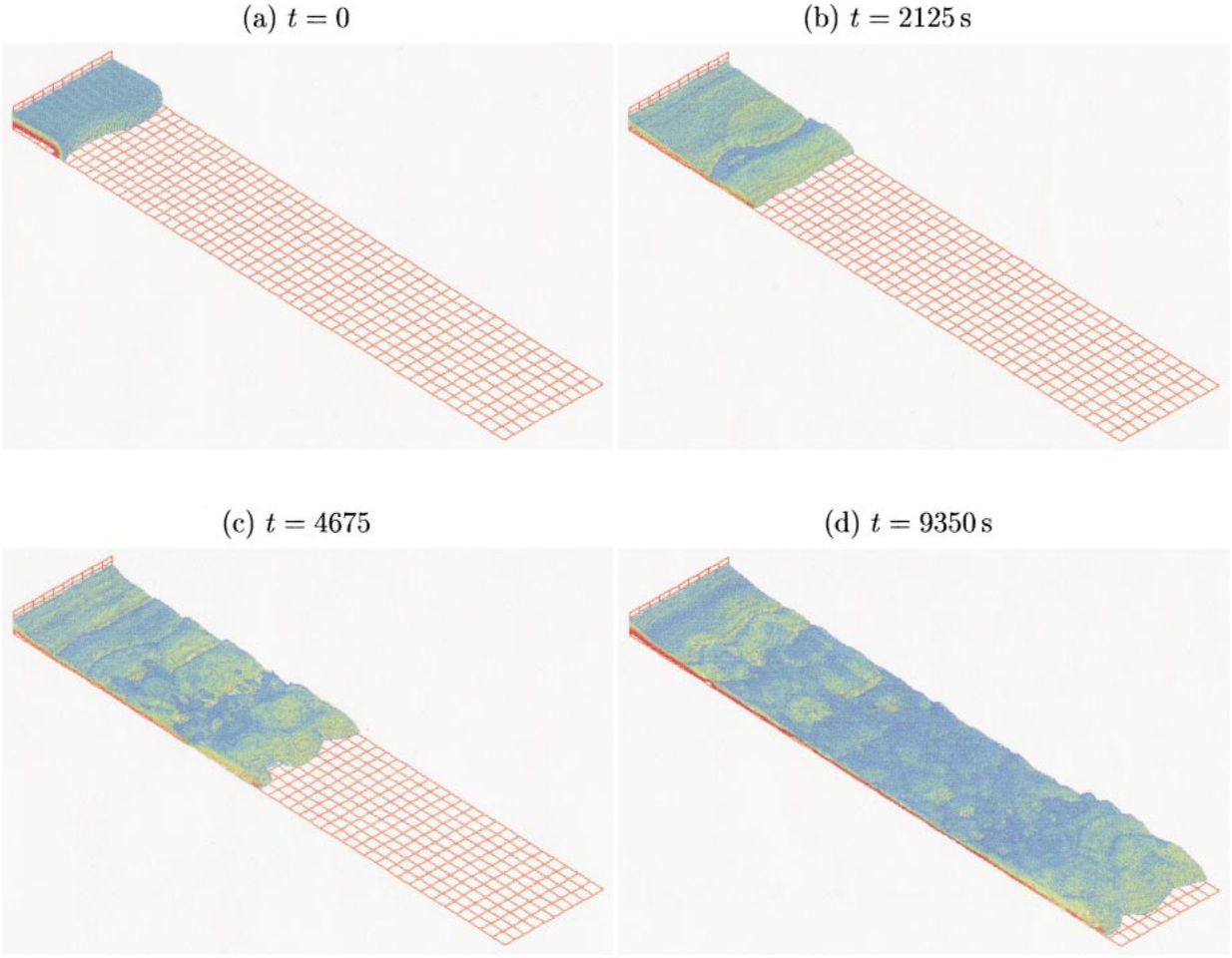

FIG. 3. Distribution of salinity surface $0.3 \leq S \leq 0.6$ in EXP-3Da at (a) $t = 0$, (b) $t = 2125$ s (≈0.6 h), (c) $t = 4675$ s (≈1.3 h), and (d) $t = 9350$ s (≈2.6 h). Color scale is in Fig. 2.

are dynamical secondary instabilities that tend to initiate in the vortex core and the interface between strongly rotational and weakly rotational fluid and that develop independently at different growth rates. Second are convective secondary instabilities in the statically unstable regions, which develop as the interface between the two streams overturns. The spanwise variation of shear instability is therefore one of the main mechanisms because of which differences in propagation speed and entrainment can exist between 2D and 3D bottom gravity current simulations.

Several streamwise sections of the salinity distribution are depicted in Fig. 4a for EXP-3Da. While individual sections exhibit coherent features similar in size to those obtained in EXP-2D, the spanwise-averaged salinity distribution actually shows less structure (Fig. 4b vs Fig. 2c) because of the variation of shear instabilities in the lateral direction.

EXP-3Db differs from EXP-3Da in that the amplitude of the initial spanwise perturbation is 3 times as large ($a = 0.3$; Fig. 5a vs Fig. 3a). This experiment is conducted to explore the sensitivity of results to this perturbation. In a qualitative sense, the description of the evolution of the system in EXP-3Db (Figs. 5b–d) follows that of EXP-3Da.

b. Speed of descent

It is well known that in lock-exchange flows (e.g., Keulegan 1958) and for constant-flux gravity currents (e.g., Ellison and Turner 1959; Britter and Linden 1980), the density front quickly reaches a constant speed of propagation. The propagation speed is insensitive to variations in slope angle, since the increase in gravitational force from the greater slope angle is compensated by buoyancy gain from increased entrainment. In order to conduct a quantitative comparison with previous laboratory and numerical results, the location of density fronts is measured from spanwise-averaged salinity distributions that are sampled every 500 time steps. The position of density fronts X_F as a function of time is shown in Fig. 6 for all experiments. In EXP-2D, the density front propagates at a remarkably constant rate, which is initially followed closely by EXP-3Da,b, but

Unauthenticated | Downloaded 12/09/24 12:22 AM UTC

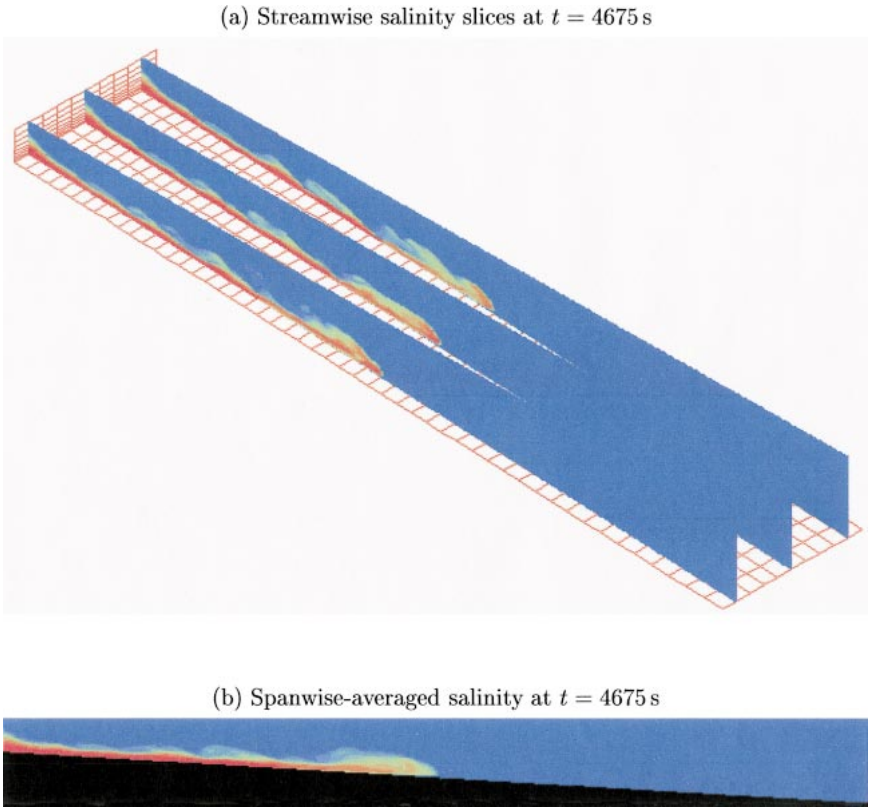

FIG. 4. (a) Streamwise slices and (b) spanwise-average of salinity distribution in EXP-3Da at $t = 4675$ s (color scale is in Fig. 2).

a transition takes place during the time interval 3000 s $\leq t \leq$ 3500 s in that the 3D experiments start deviating from the 2D case by adopting a faster rate of propagation. This time period coincides with the transition from approximately 2D to 3D instabilities in EXP-3Da,b as shown in Figs. 3b–c and 5b–c. Since the speed of propagation is closely linked with details of entrainment, Fig. 6 suggests that there is a marked shift in the nature of entrainment following the onset of 3D instabilities.

The relevant scale for the propagation speed is the speed of internal wave associated with the buoyancy input. In lock-exchange flows, the buoyancy speed scale is $\sqrt{g'h_0}$, where $g' = g\beta\Delta S \approx 7 \times 10^{-3}$ m s^{-2} is the reduced gravity and $h_0 = 200$ m is the thickness of dense water at the top of the slope, leading to a speed scale of 1.17 m s^{-1}. Even though this scale applies to flows over horizontal surfaces, given the gentle slope in this study, it is reasonable to make a comparison with this speed scale. The propagation speed is estimated from $U_F = dX_F/dt$, and the ratio $U_F/\sqrt{g'h_0}$ is plotted in Fig. 7 for all experiments. Following an initial adjustment period, EXP-2D reaches a constant propagation speed ratio of $U_F/\sqrt{g'h_0} \approx 0.73$, whereas EXP-3Da,b oscillate around a mean value of $U_F/\sqrt{g'h_0} \approx 0.85$. The 3D experiments exhibit more variation in U_F, probably because of the lobe and cleft instability at the leading edge (Figs. 3, 4). Benjamin (1968) estimated theoretically that $U_F/\sqrt{g'h_0} = 1/\sqrt{2}$ when the ratio of dense water depth and total water depth is 0.5 (as near the inlet) and $U_F/\sqrt{g'h_0} = 1$ when the depth ratio is 0.2 (as near the outlet). Figure 7 indicates that Benjamin's (1968) formulas yield reasonable bounds for the results from numerical experiments. However, we note that theoretical results are subject to a variety of assumptions, some of which are clearly unrealistic, such as neglect of friction and mixing.

It is therefore of interest to compare the speed of propagation with that from laboratory experiments. Britter and Linden (1980) found, and it also follows from dimensional analysis, that $U_F \sim (g'Q)^{1/3}$ where Q is the volume flux at the inlet. In our experiments, the boundary conditions act in a way to establish quickly a steady volume flux (spanwise averaged) of $Q \approx 125$ m^2 s^{-1} and hence yield a propagation speed scale of 0.95 m s^{-1}. The proportionality constant is estimated from Fig. 8, which shows $U_F/(g'Q)^{1/3} = 0.9$ for EXP-2D, and $U_F/(g'Q)^{1/3} \approx 1.1$ for EXP-3Da,b. These results, in particular those from 3D experiments, are in good agreement with laboratory measurements of Britter and Linden (1980), who found $U_F/(g'Q)^{1/3} = 1.5 \pm 0.2$, and of Monaghan et al. (1999), who reported $U_F/(g'Q)^{1/3} = 1.0 \pm 0.1$.

Unauthenticated | Downloaded 12/09/24 12:22 AM UTC

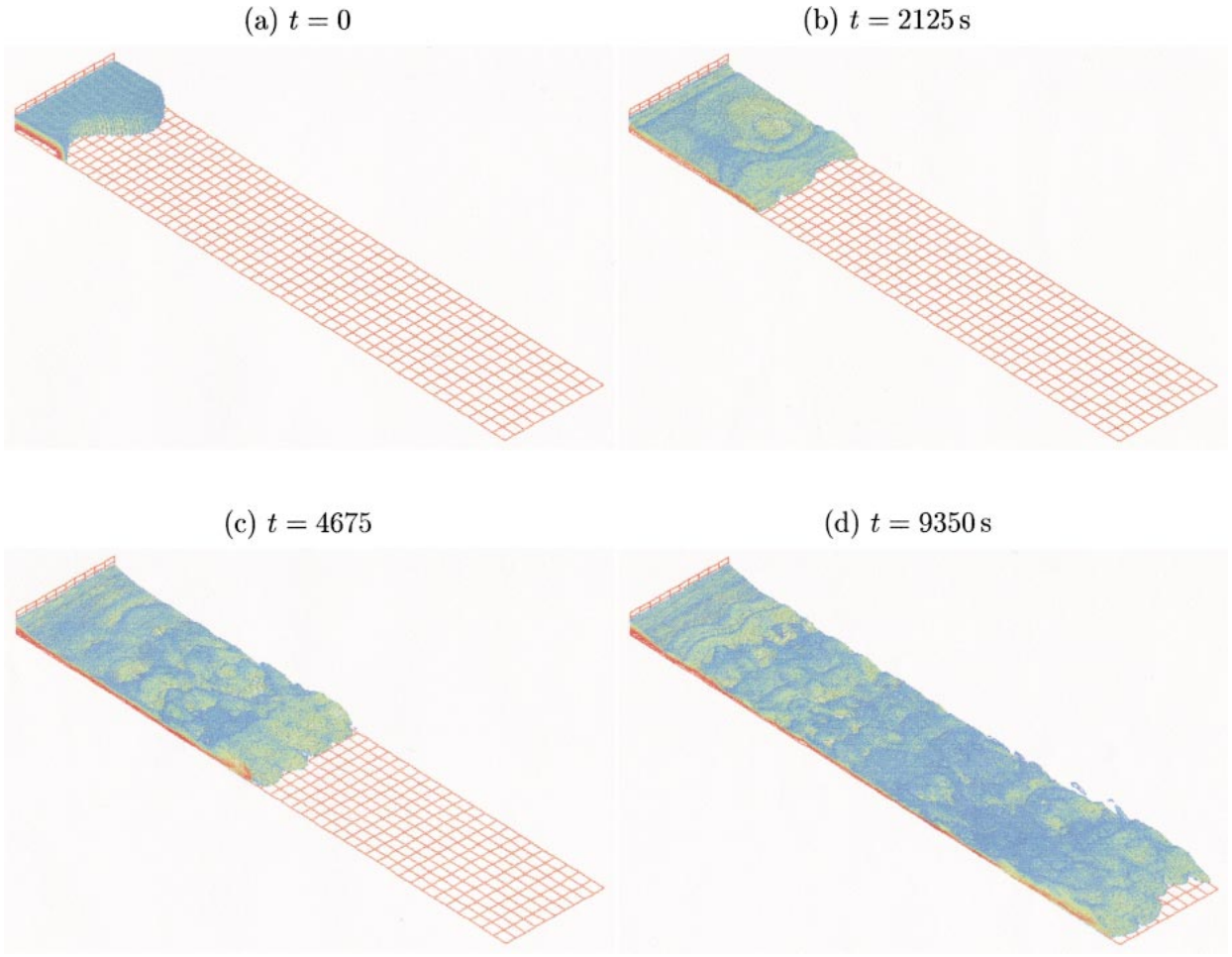

FIG. 5. Distribution of salinity surface $0.3 \leq S \leq 0.6$ in EXP-3Db at (a) $t = 0$, (b) $t = 2125$ s (≈0.6 h), (c) $t = 4675$ s (≈1.3 h), and (d) $t = 9350$ s (≈2.6 h). Color scale is in Fig. 2.

c. Characteristics of the head

The head vortex at the leading edge is a characteristic feature of the start-up phase in bottom gravity currents. The lighter fluid is displaced and lifted up by the leading edge of the gravity current, and strong entrainment takes place into the head from behind (e.g., as shown in Fig. 11 in Özgökmen and Chassignet 2002). As the head vortex carries fresh fluid from around the front to the rear of the head, this entrainment leads to the growth of the head. Therefore, it is of interest to quantify the growth rate of the head vortex.

The change in head height $\mathcal{H}$ with downslope distance X is shown in Fig. 9 for all experiments. This figure indicates that the head of the gravity current in EXP-2D grows at approximately constant rate of $d\mathcal{H}/dX \approx 0.051$. The head does not remain as a coherent structure all the way down the slope but the front vortex splits at approximately $X = 7000$ m. Following the split, the size of the front vortex becomes smaller, but it starts growing at the same rate again. This rate of growth is in very good agreement with $d\mathcal{H}/dX \approx 0.046$ obtained from the following relationship for $\theta = 3.5°$,

$$\frac{d\mathcal{H}}{dX} \approx 13 \times 10^{-3}\theta, \quad \text{for } 1° \leq \theta \leq 5°, \tag{20}$$

that was derived by Özgökmen and Chassignet (2002) based on 2D numerical experiments.

However, Ellison and Turner (1959), Britter and Linden (1980), and Monaghan et al. (1999) obtained from laboratory experiments that

$$\frac{d\mathcal{H}}{dX} \approx 4 \times 10^{-3}\theta, \tag{21}$$

and the discrepancy between (20) and (21) was surmised to be due to the 2D nature of the simulations by Özgökmen and Chassignet (2002).

As shown in Fig. 9, the growth rate of the head in EXP-3Da,b follows that in EXP-2D until $t \approx 3500$ s, as all experiments exhibit 2D characteristics during this initial phase. Once the transition to 3D takes place, how-

Unauthenticated | Downloaded 12/09/24 12:22 AM UTC

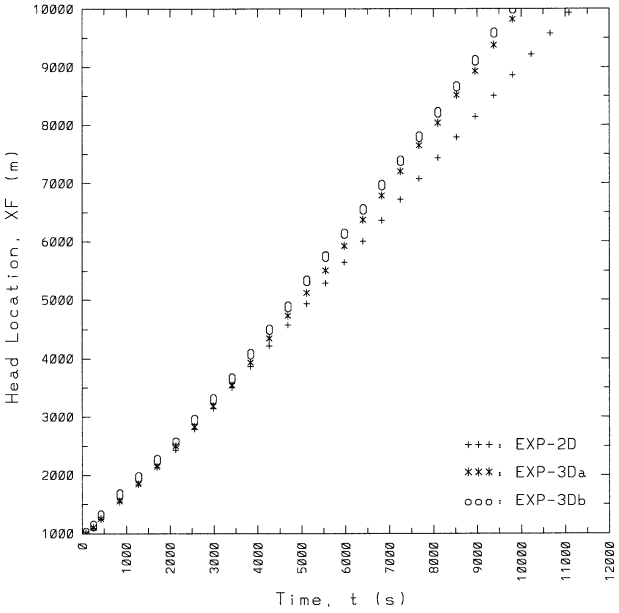

FIG. 6. Position of the density front X_F (m) as a function of time (s) in experiments EXP-2D (pluses), EXP-3Da (asterisks), and EXP-3Db (open circles).

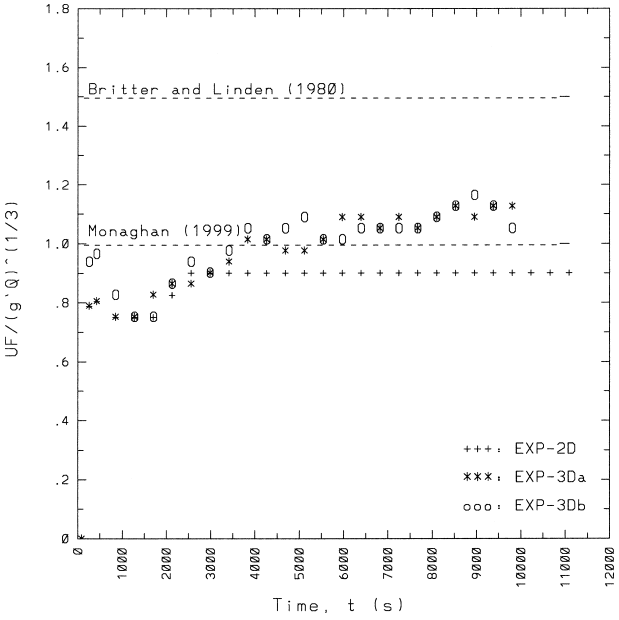

FIG. 8. Descent speed normalized by the speed of input buoyancy flux, $U_F/(g'Q)^{1/3}$. Dashed lines mark the mean values from laboratory experiments by Britter and Linden (1980): $U_F/(g'Q)^{1/3} = 1.5 \pm 0.2$, and Monaghan et al. (1999): $U_F/(g'Q)^{1/3} = 1.0 \pm 0.1$.

ever, the head growth rate slows down significantly, and a least squares fit to data points from EXP-3Da,b yields $d\mathcal{H}/dX \approx 0.015$, which is in very good agreement with $d\mathcal{H}/dX \approx 0.014$ obtained from (21) for $\theta = 3.5°$.

The lengths of head L are also estimated from the experiments. Britter and Linden (1980) demonstrate that the growth rates of the length and height of the head are directly proportional, and the aspect ratio of height versus length is a function of the slope angle. Figure 10 shows that following an initial adjustment period, the ratio $\mathcal{H}/L$ stabilizes around a mean value of

$$\frac{\mathcal{H}}{L} \approx 0.23, \tag{22}$$

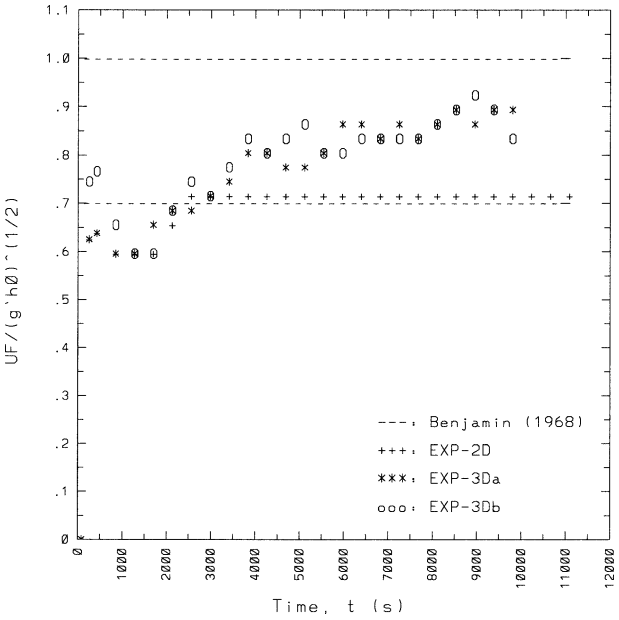

FIG. 7. Descent speed normalized by the speed of internal wave for lock-exchange flows, $U_F/\sqrt{g'h_0}$. Dashed lines show theoretical results by Benjamin (1968), who found that $U_F/\sqrt{g'h_0} = 1/\sqrt{2}$ when the ratio of dense water and total water depth is 0.5 and $U_F/\sqrt{g'h_0} = 1$ when the depth ratio is 0.2.

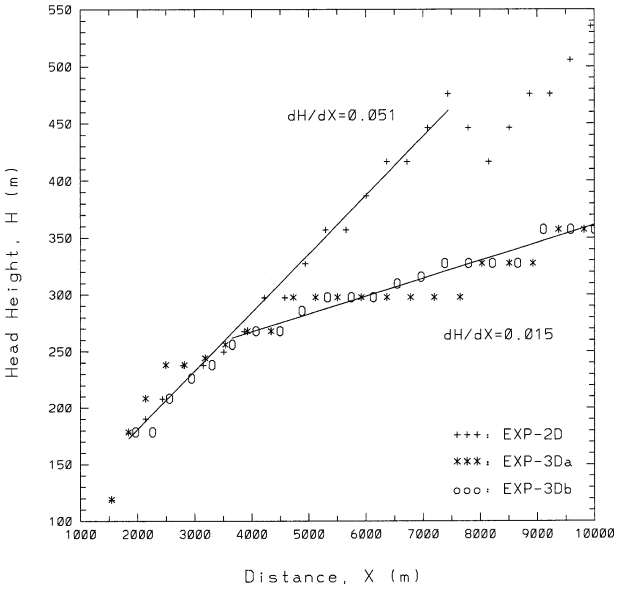

FIG. 9. Change of head height $\mathcal{H}$ (m) with distance X (m). Solid lines show least squares approximations to data points, $d\mathcal{H}/dX \approx 0.051$ for 2D phase and $d\mathcal{H}/dX \approx 0.015$ for 3D phase.

Unauthenticated | Downloaded 12/09/24 12:22 AM UTC

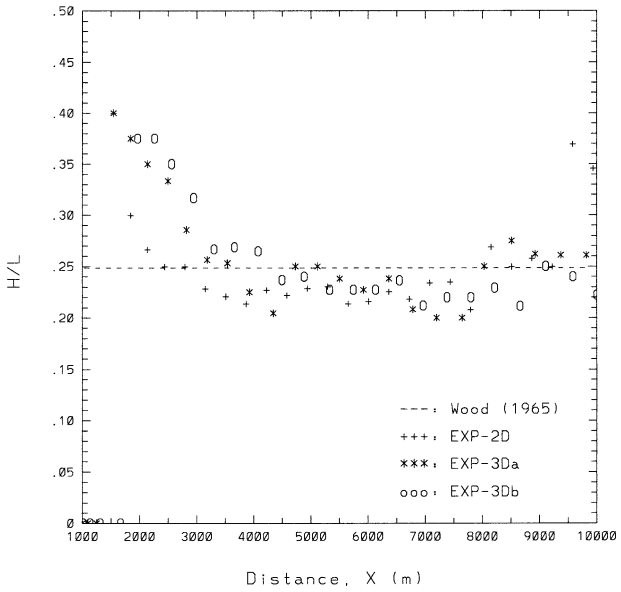

FIG. 10. Ratio of head height to head length $\mathcal{H}/L$ as a function of distance X (m). The dashed line indicates the laboratory result by Wood (1965; extracted from Fig. 9 of Britter and Linden 1980) that $\mathcal{H}/L \approx 0.25$ for gravity current over a slope of $\theta = 5°$.

which is in good agreement with the laboratory result of Wood (1965; extracted from Fig. 9 of Britter and Linden 1980) that $\mathcal{H}/L \approx 0.25$ for gravity current over a slope of $\theta = 5°$.

d. Turbulent overturning length scales

The geometric scales of the head are analyzed in section 4c, but it is of interest to quantify all turbulent scales that contribute to mixing. Several relevant length scales in stratified shear flows have been proposed and investigated in detail (e.g., Ozmidov 1965; Thorpe 1977; Dillon 1982; Osborn 1980; Itsweire et al. 1993; Smyth and Moum 2000; Tseng and Ferziger 2001). Some of these length scales require determination of background potential energy, that is, the minimum potential energy attainable through an adiabatic distribution of the density field (e.g., Winters et al. 1995). This is complicated in the present experimental setup in which boundary fluxes are permitted and a density front propagates over elevation changes. Given that the main objective is to compare turbulent length scales in 2D versus 3D, we focus on a single scale, the Thorpe scale, which is well defined, commonly used, and straightforward to compute. Thorpe's (1977) method consists of reordering a model/data density profile, which may contain inversions, into a stable monotonic profile that contains no inversions (e.g., Fig. 11a). Thorpe displacement d is the distance that the water parcel must travel vertically in order to reach neutral buoyancy (e.g., Fig.

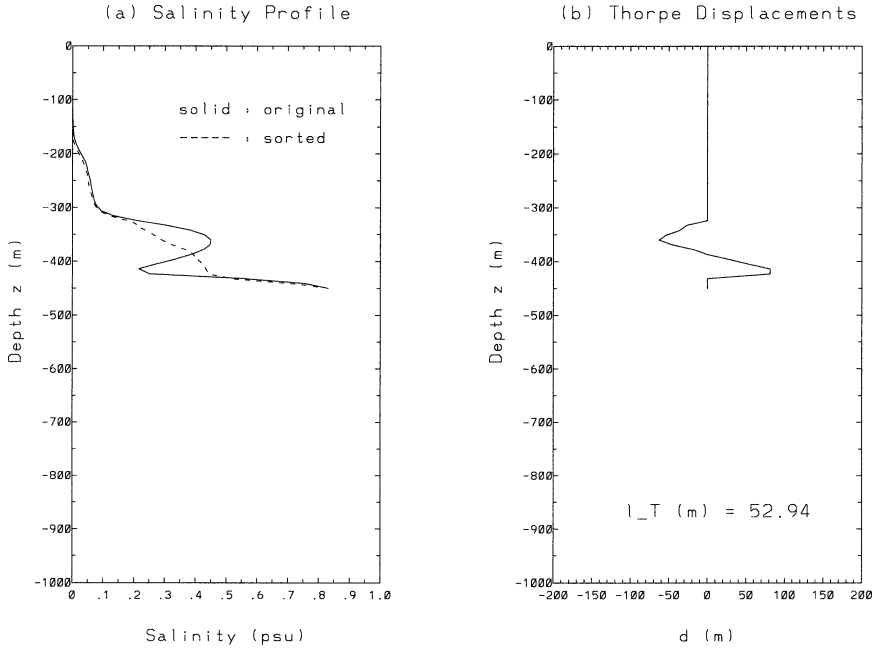

FIG. 11. (a) Sample salinity profile taken from EXP-2D at $x = 1.5$ km and $t = 9829$ s (solid line). The dashed line shows the same values after being reordered into a stable monotonic profile. (b) Thorpe displacement d indicates the distance that water parcels in the original salinity profile must travel to reach stable stratification. Thorpe scale, $\ell_T \equiv \langle d^2 \rangle_z^{1/2}$, is proportional to the scale of vertical overturning.

Unauthenticated | Downloaded 12/09/24 12:22 AM UTC

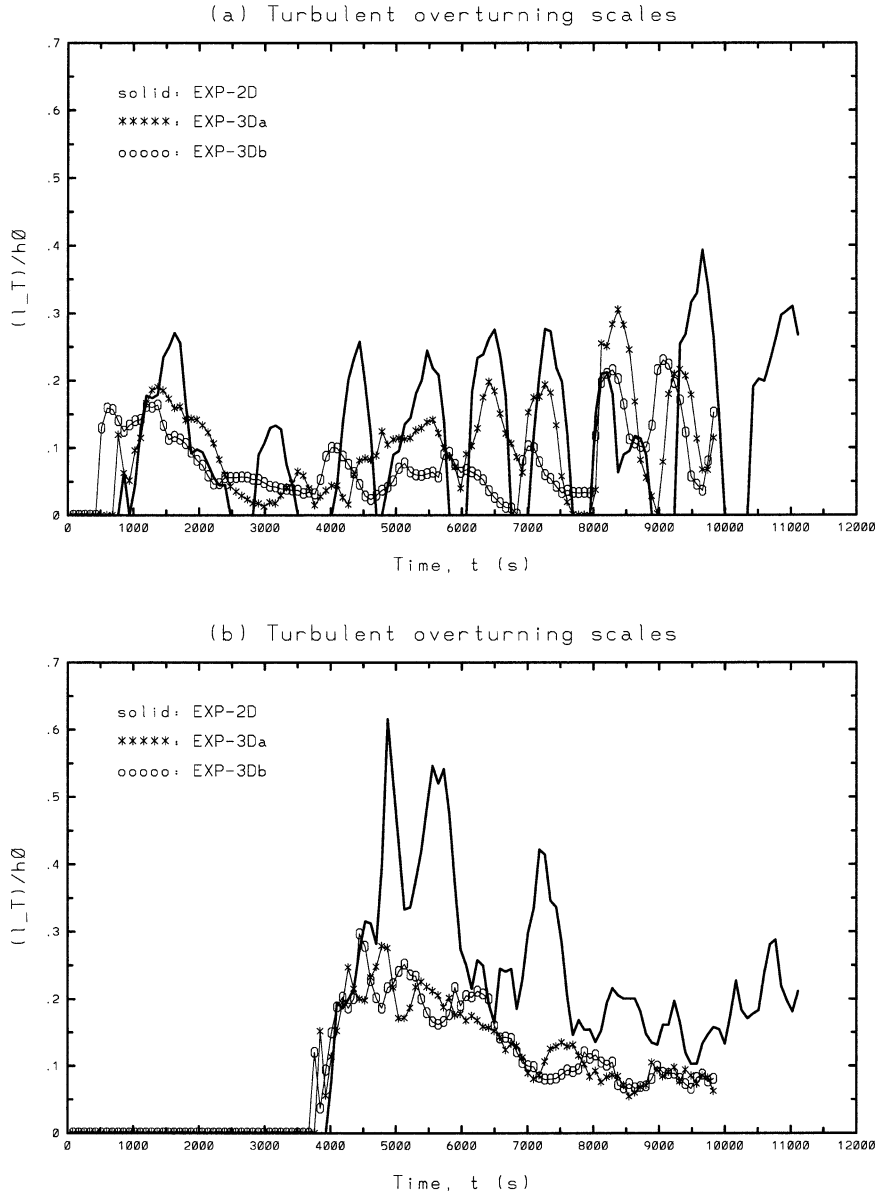

FIG. 12. Average turbulent overturning scales normalized by the initial thickness of dense water column, $(\overline{\ell_T}/h_0)$, which are sampled as a function of time at (a) $x = 1.5$ km and (b) $x = 4.0$ km in EXP-2D (solid lines), EXP-3Da (lines with asterisks), and EXP-3Db (lines with open circles). Defining a buoyancy time scale $t_b \equiv 2\pi\sqrt{h_0/g'} \approx 1061$ s, the time axis, $t = 12\,000$ s scales to $t/t_b = 11.3$.

11b). The Thorpe scale ℓ_T is defined as the rms of the displacements,

$$\ell_T = \langle d^2 \rangle_z^{1/2}, \tag{23}$$

which is proportional to the scale of the vertical overturning. It is also useful to define the horizontally averaged Thorpe scale $\overline{\ell_T}$,

$$\overline{\ell_T} = \langle \ell_T \rangle_{x,y}, \tag{24}$$

where $\langle\ \rangle$ denotes the mean and the subscripts indicate the direction.

In the numerical experiments, Thorpe scales are calculated in two ways. The first is by selecting a specific location in x and then monitoring spanwise-averaged $\overline{\ell_T}$ as the density front arrives and passes by this location. The second is by calculating $\overline{\ell_T}$ over the entire length of descending plumes. The former reveals the details of coherent structures at specific locations, whereas the latter gives an average of all turbulent scales as a function of time.

Figure 12a shows the average Thorpe scale normalized by the initial dense water depth $(\overline{\ell_T}/h_0)$ near the

Unauthenticated | Downloaded 12/09/24 12:22 AM UTC

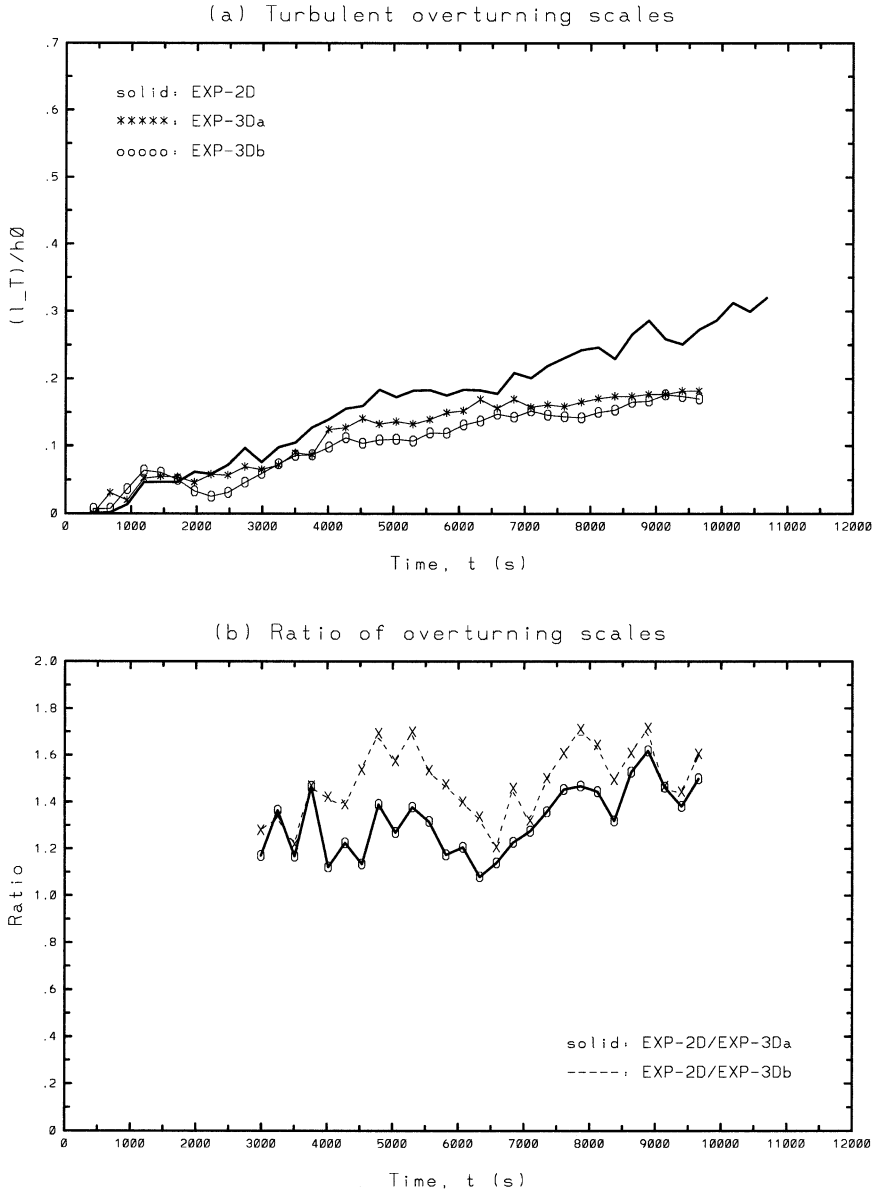

FIG. 13. (a) Turbulent overturning scales normalized by the initial thickness of dense water column, $(\overline{\ell_T}/h_0)$, which are averaged over the entire length of descending plumes in EXP-2D (solid lines), EXP-3Da (lines with asterisks), and EXP-3Db (lines with open circles). (b) The ratio of 2D and 3D overturning scales, EXP-2D/EXP-3Da (solid line) and EXP-2D/EXP-3Db (dashed line).

top of the slope at $x = 1.5$ km in all experiments as a function of time. The turbulent scales in both 2D and 3D experiments exhibit pulses of intense overturning separated by periods of laminar flow. This seems to be a manifestation of Kelvin–Helmholtz shear instabilities that tend to occur at this location, as seen in Figs. 2, 3, and 5. In addition, $(\overline{\ell_T}/h_0)$ is calculated near the middle of the slope at $x = 4.0$ km (Fig. 12b). The arrival of the large overturning scale associated with the head vortex is followed by smaller-scale overturning eddies that seem to be continuous in time rather than episodic as those at $x = 1.5$ km. Figure 12 indicates no significant difference between the scales observed in EXP-3Da and EXP-3Db, whereas those in EXP-2D appear to be somewhat larger. Turbulent scales $(\overline{\ell_T}/h_0)$ averaged over the entire length of descending plumes are shown in Fig. 13a. The growth in the overturning scale in time is due only partly to the growth of the head vortex and is inherently related to the transient nature of the experiments. Figure 13a confirms that turbulent scales averaged over the entire plume are somewhat larger in 2D than in 3D. The ratio of 2D and 3D scales is quantified

Unauthenticated | Downloaded 12/09/24 12:22 AM UTC

in Fig. 13b (after the initial transient), which indicates that, on average, turbulent scales are 30%–50% larger in EXP-2D than those in EXP-3Da,b. This difference seems to be because, as indicated by Fjortoft's (1953) theorem, 2D turbulence allows for cascade of energy toward both small and large scales, leading to a double cascading spectrum (e.g., Lesieur 1997). Physically, the inverse energy transfer to large scales results from pairing of Kelvin–Helmholtz vortices, which is well documented in 2D shear flows (e.g., Corcos and Sherman 1984; Klaassen and Peltier 1989). In 3D, the energy cascade is toward small scales, with the coherent overturning structures being created and maintained under the steady gravitational forcing in the system. Ultimately, the work done by the turbulent overturning eddies determines how much ambient fluid is entrained into the gravity currents, which is quantified in the next section.

e. Entrainment

Following the definition of Morton et al. (1956), entrainment is typically quantified as

$$E \equiv \frac{w_E}{U}, \tag{25}$$

where w_E is the net entrainment velocity and U is the local current speed. For bottom gravity currents, this can be approximated as

$$E \approx \frac{\delta h}{\ell}, \tag{26}$$

where δh is the increase (decrease) in the thickness of the dense current due to entrainment (detrainment) over a net streamwise distance of ℓ. We note that while relatively reliable estimates of ℓ or U are possible, w_E or δh can be very difficult to estimate by using profiles from individual sections, in particular for 3D data, because of the highly turbulent and time-dependent nature of the flow. Here, we define an entrainment metric that is similar to previous definitions by Meleshko and Van Heijst (1995), Hallworth et al. (1996), and Özgökmen and Chassignet (2002) but has the advantages of being a reliable estimate that applies equally well to both transient and statistically steady flows and being compatible with definitions (25) and (26):

$$E(t) \equiv \frac{V_{\text{total}}(t) - V_0(t)}{V(t)}, \tag{27}$$

where V_{total} is the total volume of dense fluid

$$V_{\text{total}}(t) \equiv \int_0^{L_y} \int_{x_0}^{X_F(y',t)} h(x', y', t)\, dx'\, dy', \tag{28}$$

between a reference station of x_0 and the leading edge of the density current X_F. Here, we take $x_0 = 1.5$ km to clear the initial volumes of the dense water in the experiments (e.g., Figs. 2a, 3a, 5a). The overflow thickness h is calculated from

$$h(x, y, t) \equiv \int_0^{z_0} \gamma(x, y, z', t)\, dz',$$

where

$$\gamma(x, y, z, t) = \begin{cases} 0, & \text{when } S(x, y, z, t) < \epsilon \\ 1, & \text{when } S(x, y, z, t) \geq \epsilon, \end{cases} \tag{29}$$

where z_0 is the depth of bottom topography, and $\epsilon = 0.2$ (psu) is the density interface threshold value, since it is the lowest density value remaining as a coherent part of the gravity current (fluid particles with lower density tend to detach from the current and be advected with the overlying counter flow). In principle, the density interface threshold value can be continuously varied to explore exchanges of fluid between different density layers; however, this is beyond the scope of our interest here. Here V_0 is the input volume of dense fluid at the reference station at the top of the slope (for small θ)

$$V_0(t) \equiv \int_0^t \int_0^{L_y} \int_{z_0+h}^{z_0} u(x_0, y', z', t')\, dz'\, dy'\, dt', \tag{30}$$

and finally

$$V(t) \equiv \overline{\ell}(t)^2 L_y, \tag{31}$$

where $\overline{\ell}(t) = \langle X_F(y, t) - x_0 \rangle_y$ is the spanwise-averaged length of the dense overflow measured from the reference station x_0.

Noting that

$$V_{\text{total}}(t) = \overline{h}(t)\overline{\ell}(t)L_y \quad \text{and} \tag{32}$$

$$V_0(t) = \overline{h}_0(t)\overline{\ell}(t)L_y, \tag{33}$$

where $\overline{h}(t)$ and $\overline{h}_0(t)$ are the total (with entrainment) and original (without any entrainment) mean thickness of dense water, we can write (27) as

$$E(t) = \frac{\overline{h}(t) - \overline{h}_0(t)}{\overline{\ell}(t)}. \tag{34}$$

It can be seen that (34) is compatible with traditional definitions (25) and (26), but estimation of $\overline{h}(t)$and $\overline{h}_0(t)$ from volume integrals (28) and (30) leads to reliable estimates of E. (In 2D, integration in the y direction is not necessary, and volume integrals reduce to area integrals.)

Figure 14 depicts time evolutions of $\overline{h}(t)$ and $\overline{h}_0(t)$ in EXP-2D. Since there is no entrainment initially, $\overline{h}_0 \approx \overline{h}$. Once the head starts forming during 1500 s $\leq t \leq$ 2500 s, these quantities start to differ. We note that $\overline{h}_0$ stabilizes around a mean value of 150 m, whereas $\overline{h}$ shows a steady increase because of entrainment. Similar behavior follows in the other experiments (not shown).

Time evolutions of entrainment parameters $E(t)$ in all experiments are shown in Fig. 15. Entrainment starts at

Unauthenticated | Downloaded 12/09/24 12:22 AM UTC

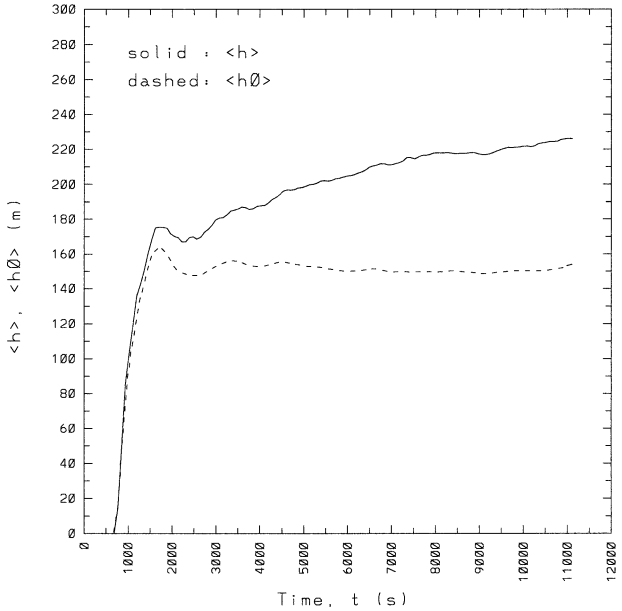

FIG. 14. Time evolution of original mean overflow thickness $\overline{h_0}(t)$ and total mean overflow thickness $\overline{h}(t)$ in EXP-2D. Note that $\overline{h_0} \approx \overline{h}$ until the initial formation of the head during 1500 s $\leq t \leq$ 2500 s and then $\overline{h_0}$ stabilizes around a mean value of 150 m whereas $\overline{h}$ shows a steady increase because of entrainment.

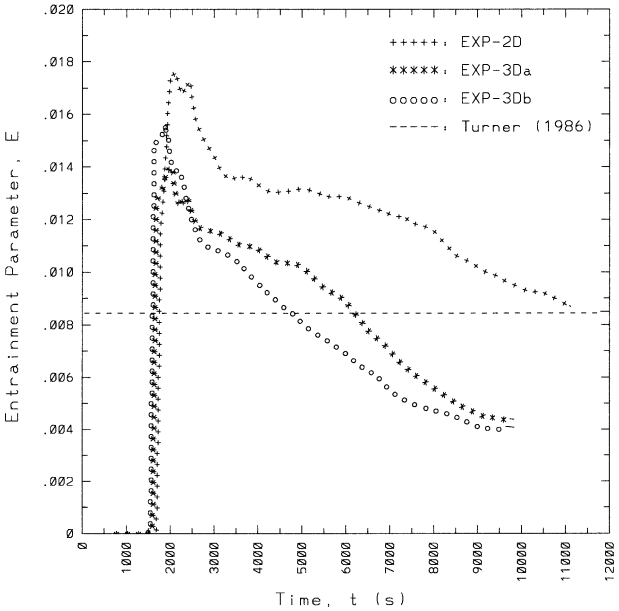

FIG. 15. Time evolution of entrainment parameters $E(t)$ in all experiments. Dashed line marks the estimate $E = (5 + \theta) \times 10^{-3} = 0.0085$ given by Turner (1986) based on laboratory experiments of Ellison and Turner (1959).

slightly different times because of differences in the initialization of the experiments. The initial entrainment rates are quite comparable because of the 2D nature of the flow during initial stages, as discussed earlier. Entrainment parameter decreases in time in all experiments, because initially entrainment is associated with the growth of the head, which is known to be higher than that in the trailing flow (e.g., Turner 1986). As the gravity current flows down the slope, the contribution of the head entrainment to overall entrainment decreases. Entrainment in 3D experiments decreases at a faster rate than that in EXP-2D partly because the head starts showing 3D characteristics after $t > 3000$ s (Fig. 9) and grows at a smaller rate, as discussed in section 4c. In general, it is not surprising that the entrainment during the start-up phase is higher than that in a phase approaching equilibrium (e.g., Beckmann 1998). It is worth noting that the Thorpe scales are somewhat smaller in EXP-3Db than those in EXP-3Da (Fig. 13), and consequently entrainment parameter E is also slightly smaller in EXP-3Db (Fig. 15). As the only difference between these experiments is the initial conditions (Fig. 3a vs 5a), we conclude that the currents do not totally decorrelate from the initial conditions over most of the slope. However the results from both experiments are converging in the second half of the integration (for $t > 7000$ s; Figs. 13, 15), and the difference in E between EXP-3Da and EXP-3Db is much smaller than those between EXP-3Da,b and EXP-2D. By the end of the integrations, E in EXP-2D is approximately 2 times those from EXP-3Da,b, which is consistent with the results found about differences in turbulent length scales in section 4d. For reference, the estimate $E = (5 + \theta) \times 10^{-3}$ given by Turner (1986) based on laboratory experiments of Ellison and Turner (1959) is plotted in Fig. 15 as well. Note, however, that the actual laboratory experiments were conducted for $\theta > 10°$ and the above relationship is extended to $\theta = 3.5°$ in this study. The entrainment parameter in 3D experiments is $E \approx 5 \times 10^{-3}$ at the end of the integrations, but possibly still decreasing. This is somewhat higher than the entrainment parameters observed in oceanic overflows, which are estimated to be in the range of $0.2 \times 10^{-3} \leq E \leq 2 \times 10^{-3}$ (Baringer and Price 1997b: based on Mediterranean Sea overflow observations; Özgökmen et al. 2003: based on Red Sea overflow observations and numerical modeling). However, the high entrainment in the numerical experiments could be due to a variety of factors, including the time-dependent nature of the flow, differences in slope angles, the neglect of rotation and ambient stratification, and generally, the idealized nature of this investigation.

5. Summary and conclusions

This study is motivated by the fact that most deep and intermediate water masses are released into the large-scale ocean circulation from high-latitude and marginal seas in the form of overflows. In light of observations that revealed that the mixing of overflows with the ambient fluid takes place over very small spatial and time scales (Price et al. 1993; Baringer and Price 1997a,b; Price and Yang 1998), and studies with ocean

Unauthenticated | Downloaded 12/09/24 12:22 AM UTC

general circulation models that demonstrated that the strength of the thermohaline circulation is very sensitive to details of the representation of overflows in these models (e.g., Willebrand et al. 2001), overflow-induced entrainment is being generally recognized as one of the prominent oceanic processes. The importance of overflows has led to significant effort to improve their representation in ocean models, and significant progress has been achieved recently (e.g., Beckmann and Döscher 1997; Winton et al. 1998; Killworth and Edwards 1999; Jungclaus and Mellor 2000; Hallberg 2000; Nakano and Suginohara 2002; Papadakis et al. 2003).

Process modeling is an important avenue that will complement dedicated observational programs such as those in the Meditteranean Sea (Price et al. 1993) the Red Sea (Bower et al. 2002; Peters et al. 2004) and the Denmark Strait (Girton et al. 2001) in order to improve parameterizations of overflow processes. However, because of the small space and time scales, exploration of overflow processes demands high-resolution, nonhydrostatic models. In recent nonhydrostatic simulations of bottom gravity currents in idealized (Özgökmen and Chassignet 2002) and realistic (Özgökmen et al. 2003) settings, a 2D model was used, which offers great simplicity and computational efficiency, albeit at the expense of allowing only the spanwise component of vorticity and thus potentially modifying the ways in which mixing and entrainment can take place in a real fluid. Therefore, a logical next step is to conduct 3D numerical experiments. Our primary objective in this study is to explore differences between 2D and 3D nonhydrostatic simulations bottom gravity currents.

Three-dimensional nonhydrostatic experiments are facilitated greatly by the use of a sophisticated numerical model that has good convergence characteristics to minimize the number of grid points and time steps, and good scalability on parallel computers. Spectral-element models provide characteristics such as minimal numerical dissipation and excellent scalability. Spectral-element design combines the geometric flexibility of finite-element models with the numerical accuracy of spectral decomposition. It also offers a dual approach to convergence: algebraic via elemental grid refinement and exponential via the increase in the order of intra-element interpolation. The use of the spectral-element method for ocean general circulation (hydrostatic) simulations has been pioneered by Iskandarani et al. (1995, 2002, 2003). Here we use a high-order spectral-element Navier-Stokes solver (documented in detail in Fischer 1997; Fischer et al. 2000; Tufo and Fischer 1999; Fischer and Mullen 2001) as the basis for our nonhydrostatic simulations.

The initial evolution of a dense water mass released at the top of a sloping wedge at a constant angle is explored. Results from a 2D turbulent simulation, denoted EXP-2D, are compared with those from equivalent 3D simulations, denoted EXP-3Da,b, that are conducted by extending the domain in the spanwise direction. The 3D experiments differ only in the magnitude of the initial spanwise perturbation that is used to facilitate 3D breakdown. No significant difference is found between the results from the two 3D experiments, but they provide two different realizations, thus increasing the reliability of the results. To our knowledge, the present numerical simulations are the first to capture explicitly 3D shear instability in bottom gravity currents propagating over a sloping topography.

Qualitatively, evolutions of bottom gravity currents in 2D and 3D are similar, both exhibiting a large vortex in the leading edge and shear instabilities in the trailing fluid. In 3D experiments, both the head vortex and Kelvin–Helmholtz rolls show 2D characteristics spanning the entire width of the domain but then make a transition to 3D by exhibiting a breakdown of spanwise rolls and the so-called lobe and cleft instability in the leading edge, which is caused by the instability associated with the nose propagation (Härtel et al. 2000) and is a well-known feature from laboratory experiments (e.g., Simpson 1972).

Quantitatively, the propagation speed of the density front is $U_F/(g'Q)^{1/3} \approx 0.9$ (or $U_F = 0.85$ m s^{-1}) in EXP-2D and $U_F/(g'Q)^{1/3} \approx 1.1$(or $U_F = 1.0$ m s^{-1}) in EXP-3Da,b, which are in good general agreement with laboratory results of $(1 \pm 0.1) \leq U_F/(g'Q)^{1/3} \leq (1.5 \pm 0.2)$ (Britter and Linden 1980; Monaghan et al. 1999) and analytical estimates of Benjamin (1968). The growth rate of the head is $d\mathcal{H}/dX \approx 0.051$ in EXP-2D, in good agreement with the relationship $d\mathcal{H}/dX \approx 13 \times 10^{-3}\,\theta \approx 0.046$ derived by Özgökmen and Chassignet (2002) based on 2D simulations. However, $d\mathcal{H}/dX \approx 0.015$ in EXP-3Da,b, in very good agreement with $d\mathcal{H}/dX \approx 4 \times 10^{-3}\,\theta \approx 0.014$ based on laboratory experiments by Ellison and Turner (1959), Britter and Linden (1980), and Monaghan et al. (1999). Hence, the head growth rate is 3 times as large in 2D as in 3D. To explore differences in turbulent length scales, Thorpe scales are calculated, which are found to be 1.3–1.5 times as large in 2D as those in 3D. The difference is scales results from cascade of energy to large scales in 2D turbulence.

Differences in the speed of propagation, head growth rates, and turbulent length scales clearly point toward differences in the entrainment characteristics in 2D and 3D. A method for a reliable estimation of entrainment parameter E is introduced that applies equally well to transient and statistically steady flows, is compatible with traditional definitions of entrainment, and is suitable for processing large data sets in 2D or 3D. It is shown that E in EXP-2D can be 2 times that in EXP-3Da,b. In absolute terms, $E \approx 5 \times 10^{-3}$ in EXP-3Da,b, which compares reasonably well with $E \approx 8.5 \times 10^{-3}$ based on a relationship given by Turner (1986), when extended to the slope angle of this study. The entrainment parameter in the numerical experiments is somewhat higher than those observed in oceanic overflows, which are typically in the range of $0.2 \times 10^{-3} \leq E \leq 2 \times 10^{-3}$. This discrepancy could be explained by a

Unauthenticated | Downloaded 12/09/24 12:22 AM UTC

variety of factors that include the time-dependent nature of the flow, differences in slope angles, the neglect of rotation and ambient stratification, and, generally, the idealized nature of this investigation.

In conclusion, although some differences between 2D and 3D simulations, which arise entirely because of internal factors associated with the truncation of the Navier–Stokes equations for 2D approximation, can be significant in a quantitative sense, 2D results are qualitatively still very close to those from 3D simulations. Therefore, in the absence of external factors that can trigger 3D circulation patterns, such as topographic variations in the spanwise direction and rotation, 2D approximation provides a computationally inexpensive approach to investigate the general behavior of bottom gravity currents. We surmise that far more significant differences between 2D and 3D results would arise in cases in which topographic slope varies in the spanwise direction or rotational effects are important. These topics will be investigated in the near future.

Acknowledgments. We greatly appreciate the support of the National Science Foundation through Grants DMS 0209326 and OCE 0336799, the Office of Naval Research through Grant N00014-03-1-0425, and the Mathematical, Information, and Computational Sciences Division subprogram of the Office of Advanced Scientific Computing Research, U.S. Department of Energy, under Contract W-31-109-ENG-38. Earlier versions of the manuscript benefited greatly from comments by Bill Johns, Mohamed Iskandarani, Pearl Bongolan Walsh, and technical editing by Gail Pieper and Judy Beumer. We thank Ashwanth Shrinivasan for the design, construction, and maintenance of the computer cluster used to run the numerical experiments.

REFERENCES

Baines, P. G., 2001: Mixing in flows down gentle slopes into stratified environments. *J. Fluid Mech.,* **443,** 237–270.

Baringer, M. O., and J. F. Price, 1997a: Mixing and spreading of the Mediterranean outflow. *J. Phys. Oceanogr.,* **27,** 1654–1677.

——, and ——, 1997b: Momentum and energy balance of the Mediterranean outflow. *J. Phys. Oceanogr.,* **27,** 1678–1692.

Beckmann, A., 1998: The representation of bottom boundary layer processes in numerical ocean circulation models. *Ocean Modeling and Parameterization,* E. P. Chassignet and J. Verron, Eds., Kluwer Academic, 135–154.

——, and R. Döscher, 1997: A method for improved representation of dense water spreading over topography in geopotential-coordinate models. *J. Phys. Oceanogr.,* **27,** 581–591.

Benjamin, T. B., 1968: Gravity currents and related phenomena. *J. Fluid Mech.,* **31,** 209–248.

Borenäs, K. M., and P. A. Lundberg, 1988: On the deep-water flow through the Faroe Bank Channel. *J. Geophys. Res.,* **93,** 1281–1292.

Bower, A. S., H. D. Hunt, and J. F. Price, 2000: Character and dynamics of the Red Sea and Persian Gulf outflows. *J. Geophys. Res.,* **105,** 6387–6414.

——, D. M. Fratantoni, W. E. Johns, and H. Peters, 2002: Gulf of Aden eddies and their impact on Red Sea Water. *Geophys. Res. Lett.,* **29,** 2025, doi:10.1029/2002GL015342.

Britter, R. E., and P. F. Linden, 1980: The motion of the front of a gravity current traveling down an incline. *J. Fluid Mech.,* **99,** 531–543.

Bryden, H. L., and T. H. Kinder, 1991: Steady two-layer exchange through the Strait of Gibraltar. *Deep-Sea Res.,* **38** (Suppl.), S445–S463.

Corcos, G. M., and F. S. Sherman, 1984: The mixing layer: Deterministic models of a turbulent flow. Part 1. Introduction and the two-dimensional flow. *J. Fluid Mech.,* **139,** 29–65.

Deville, M. O., P. F. Fischer, and E. H. Mund, 2002: *High-Order Methods for Incompressible Fluid Flow*. Cambridge University Press, 499 pp.

Dickson, R. R., E. M. Gmitrowics, and A. J. Watson, 1990: Deep water renewal in the northern North Atlantic. *Nature,* **344,** 848–850.

Dillon, T. M., 1982: Vertical overturns: A comparison of Thorpe and Ozmidov length scales. *J. Geophys. Res.,* **87,** 9601–9613.

Dryja, M., and O. B. Widlund, 1987: An additive variant of the Schwarz alternating method for the case of many subregions. Dept. of Computer Science, Courant Institute Tech. Rep. 339.

Ellison, T. H., and J. S. Turner, 1959: Turbulent entrainment in stratified flows. *J. Fluid Mech.,* **6,** 423–448.

Fischer, P. F., 1997: An overlapping Schwarz method for spectral element solution of the incompressible Navier–Stokes equations. *J. Comput. Phys.,* **133,** 84–101.

——, and J. S. Mullen, 2001: Filter-based stabilization of spectral element methods. *C. R. Acad. Sci. Paris,* **332,** 265–270.

——, N. I. Miller, and H. M. Tufo, 2000: An overlapping Schwarz method for spectral element simulation of three-dimensional incompressible flows. *Parallel Solution of Partial Differential Equations,* P. Björstad and M. Luskin, Eds., Springer-Verlag, 159–181.

Fjortoft, R., 1953: On the changes in the spectral distribution of kinetic energy for two-dimensional non-divergent flow. *Tellus,* **5,** 225–230.

Flierl, G. R., M. E. Stern, and J. A. Whitehead, 1981: The physical significance of modons: Laboratory experiments and general integral constraints. *Dyn. Atmos. Oceans,* **7,** 233–263.

Gawarkiewicz, G., and D. C. Chapman, 1995: A numerical study of dense water formation and transport on a shallow, sloping continental shelf. *J. Geophys. Res.,* **100,** 4489–4507.

Girton, J. B., T. B. Sanford, and R. H. Käse, 2001: Synoptic sections of the Denmark Strait overflow. *Geophys. Res. Lett.,* **28,** 1619–1622.

Griffiths, R. W., 1986: Gravity currents in rotating systems. *Annu. Rev. Fluid Mech.,* **18,** 59–89.

Hallberg, R., 2000: Time integration of diapycnal diffusion and Richardson number–dependent mixing in isopycnal coordinate ocean models. *Mon. Wea. Rev.,* **128,** 1402–1419.

Hallworth, M. A., H. E. Huppert, J. C. Phillips, and S. J. Sparks, 1996: Entrainment into two-dimensional and axisymmetric turbulent gravity currents. *J. Fluid Mech.,* **308,** 289–311.

Härtel, C., E. Meiburg, and F. Necker, 2000: Analysis and direct numerical simulation of the flow at a gravity-current head. Part 1: Flow topology and front speed for slip and no-slip boundaries. *J. Fluid Mech.,* **418,** 189–212.

Houze, R. A., 1993: *Cloud Dynamics*. Academic Press, 573 pp.

Iskandarani, M., D. B. Haidvogel, and J. P. Boyd, 1995: A staggered spectral element model with application to the oceanic shallow-water equations. *Int. J. Numer. Methods Fluids,* **20,** 393–414.

——, ——, J. C. Levin, E. Curchitser, and C. A. Edwards, 2002: Multiscale geophysical modeling using the spectral element method. *Comput. Sci. Eng.,* **4/5,** 42–48.

——, ——, and ——, 2003: A three-dimensional spectral element model for the solution of the hydrostatic primitive equations. *J. Comput. Phys.,* **186,** 397–425.

Itsweire, E. C., J. R. Koseff, D. A. Briggs, and J. H. Ferziger, 1993: Turbulence in stratified shear flows: Implications for interpreting shear-induced mixing in the ocean. *J. Phys. Oceanogr.,* **23,** 1508–1522.

Jia, Y., 2000: Formation of an Azores Current due to Mediterranean overflow in a modeling study of the North Atlantic. *J. Phys. Oceanogr.,* **30,** 2342–2358.

Unauthenticated | Downloaded 12/09/24 12:22 AM UTC

Jiang, L., and R. W. Garwood Jr., 1995: A numerical study of three-dimensional dense bottom plumes on a southern ocean continental slope. *J. Geophys. Res.,* **100,** 18 471–18 488.
——, and ——, 1996: Three-dimensional simulations of overflows on continental slopes. *J. Phys. Oceanogr.,* **26,** 1214–1233.
——, and ——, 1998: Effects of topographic steering and ambient stratification on overflows on continental slopes: A model study. *J. Geophys. Res.,* **103,** 5459–5476.
Jungclaus, J. H., and J. O. Backhaus, 1994: Application of a transient reduced gravity plume model to the Denmark Strait overflow. *J. Geophys. Res.,* **99,** 12 375–12 396.
——, and G. Mellor, 2000: A three-dimensional model study of the Mediterranean outflow. *J. Mar. Syst.,* **24,** 41–66.
Keulegan, G. H., 1958: The motion of saline fronts in still water. U.S. National Bureau of Standards Rep. 5831, 29 pp.
Killworth, P. D., 1977: Mixing on the Weddell Sea continental slope. *Deep-Sea Res.,* **24,** 427–448.
——, and N. R. Edwards, 1999: A turbulent bottom boundary layer code for use in numerical ocean models. *J. Phys. Oceanogr.,* **29,** 1221–1238.
Kirby, R. M., and G. E. Karniadakis, 2003: De-aliasing on non-uniform grids: Algorithms and applications. *J. Comput. Phys.,* **191,** 249–264.
Klaassen, G. P., and W. R. Peltier, 1989: The role of transverse secondary instabilities in the evolution of free shear layers. *J. Fluid Mech.,* **202,** 367–402.
——, and ——, 1991: The influence of stratification on secondary instability in free shear layers. *J. Fluid Mech.,* **227,** 71–106.
Lesieur, M., 1997: *Turbulence in Fluids.* 3d ed. Kluwer, 515 pp.
Lozier, M. S., W. B. Owens, and R. G. Curry, 1995: The climatology of the North Atlantic. *Progress in Oceanography,* Vol. 36, Pergamon, 1–44.
Maday, Y., and A. T. Patera, 1989: Spectral element methods for the Navier–Stokes equations. *State-of-the-Art Surveys in Computational Mechanics,* A. K. Noor and J. T. Oden, Eds., ASME, 71–143.
——, ——, and E. M. Rønquist, 1990: An operator-integration-factor splitting method for time-dependent problems: Application to incompressible fluid flow. *J. Sci. Comput.,* **5,** 310–337.
Marmorino, G. O., 1987: Observations of small-scale mixing processes in the seasonal thermocline. Part II: Wave breaking. *J. Phys. Oceanogr.,* **17,** 1348–1355.
Meleshko, V. V., and G. J. F. Van Heijst, 1995: Interacting two-dimensional vortex structures: Point vortices, contour kinematics and stirring properties. *Chaos Applied to Fluid Mixing,* H. Aref and M. S. El Naschie, Eds., Pergamon, 233–266.
Mellor, G. L., and T. Yamada, 1982: Development of a turbulence closure model for geophysical fluid problems. *Rev. Geophys. Space Phys.,* **20,** 851–875.
Monaghan, J. J., R. A. F. Cas, A. M. Kos, and M. Hallworth, 1999: Gravity currents descending a ramp in a stratified tank. *J. Fluid Mech.,* **379,** 39–70.
Morton, B. R., G. I. Taylor, and J. S. Turner, 1956: Turbulent gravitational convection from maintained and instantaneous sources. *Proc. Roy. Soc. London,* **A234,** 1–23.
Murray, S. P., and W. E. Johns, 1997: Direct observations of seasonal exchange through the Bab el Mandab Strait. *Geophys. Res. Lett.,* **24,** 2557–2560.
Nakano, H., and N. Suginohara, 2002: Effects of bottom boundary layer parameterization on reproducing deep and bottom waters in a World Ocean model. *J. Phys. Oceanogr.,* **32,** 1209–1227.
Nielsen, A. H., and J. J. Rasmussen, 1996: Formation and temporal evolution of the Lamb-dipole. *Phys. Fluids,* **9,** 982–991.
Orszag, S. A., 1972: Comparison of pseudospectral and spectral approximation. *Stud. Appl. Math.,* **3,** 253–259.
Osborn, T. R., 1980: Estimates of the local rate of vertical diffusion from dissipation measurements. *J. Phys. Oceanogr.,* **10,** 83–89.
Özgökmen, T. M., and F. Crisciani, 2001: On the dynamics of β plumes. *J. Phys. Oceanogr.,* **31,** 3569–3580.
——, and E. Chassignet, 2002: Dynamics of two-dimensional turbulent bottom gravity currents. *J. Phys. Oceanogr.,* **32,** 1460–1478.
——, ——, and C. G. H. Rooth, 2001: On the connection between the Mediterranean outflow and the Azores Current. *J. Phys. Oceanogr.,* **31,** 461–480.
——, W. Johns, H. Peters, and S. Matt, 2003: Turbulent mixing in the Red Sea outflow plume from a high-resolution nonhydrostatic model. *J. Phys. Oceanogr.,* **33,** 1846–1869.
Ozmidov, R. V., 1965: On the turbulent exchange in a stably stratified ocean. *Izv. Acad. Sci. USSR, Atmos. Oceanic Phys.,* **1,** 853–860.
Özsoy, E., D. D. Iorio, M. C. Gregg, and J. O. Backhaus, 2001: Mixing in the Bosphorus Strait and the Black Sea continental shelf: Observations and a model of the dense outflow. *J. Mar. Syst.,* **31,** 99–135.
Papadakis, M. P., E. P. Chassignet, and R. W. Hallberg, 2003: Numerical simulations of the Mediterranean Sea outflow: Impact of the entrainment parameterization in an isopycnic coordinate ocean model. *Ocean Modell.,* **5,** 325–356.
Patera, A. T., 1984: A spectral element method for fluid dynamics: Laminar flow in a channel expansion. *J. Comput. Phys.,* **54,** 468–488.
Peters, H., W. E. Johns, A. S. Bower, and D. M. Fratantoni, 2004: Mixing and entrainment in the Red Sea outflow plume. Part II: Turbulence characteristics. *J. Phys. Oceanogr.,* in press.
Pironneau, O., 1982: On the transport–diffusion algorithm and its applications to the Navier–Stokes equations. *J. Numer. Math.,* **38,** 309–332.
Price, J., and J. Yang, 1998: Marginal sea overflows for climate simulations. *Ocean Modeling and Parameterization,* E. P. Chassignet and J. Verron, Eds., Kluwer Academic, 155–170.
——, and Coauthors, 1993: Mediterranean outflow mixing and dynamics. *Science,* **259,** 1277–1282.
Simpson, J. E., 1969: A comparison between laboratory and atmospheric density currents. *Quart. J. Roy. Meteor. Soc.,* **95,** 758–765.
——, 1972: Effects of the lower boundary on the head of a gravity current. *J. Fluid Mech.,* **53,** 759–768.
——, 1982: Gravity currents in the laboratory, atmosphere, and the ocean. *Annu. Rev. Fluid Mech.,* **14,** 213–234.
——, 1987: *Gravity Currents in the Environment and the Laboratory.* John Wiley and Sons, 244 pp.
Smith, P. C., 1975: A streamtube model for bottom boundary currents in the ocean. *Deep-Sea Res.,* **22,** 853–873.
Smith, R. A., 1991: Maximization of vortex entropy as an organizing principle in intermittent, decaying, two-dimensional turbulence. *Phys. Rev.,* **A43,** 1126–1129.
Smyth, W. D., and J. N. Moum, 2000: Length scales of turbulence in stably stratified mixing layers. *Phys. Fluids,* **12,** 1327–1342.
Thorpe, S. A., 1977: Turbulence and mixing in a Scottish loch. *Philos. Trans. Roy. Soc. London,* **A286,** 125–181.
Tseng, Y., and J. H. Ferziger, 2001: Mixing and available potential energy in stratified flows. *Phys. Fluids,* **13,** 1281–1293.
Tufo, H. M., and P. F. Fischer, 1999: Terascale spectral element algorithms and implementations. *Proc. SC99 Conf. on High Performance Networking and Computing,* Portland, OR, ACM/IEEE, CD-ROM.
Turner, J. S., 1986: Turbulent entrainment: The development of the entrainment assumption, and its applications to geophysical flows. *J. Fluid Mech.,* **173,** 431–471.
Webster, C. A. G., 1964: An experimental study of turbulence in a density stratified shear flow. *J. Fluid Mech.,* **19,** 221–245.
Willebrand, J., and Coauthors, 2001: Circulation characteristics in three eddy-permitting models of the North Atlantic. *Progress in Oceanography,* Vol. 48, Pergamon, 123–161.
Winters, K. B., P. N. Lombard, J. J. Riley, and E. A. D'Asaro, 1995: Available potential energy and mixing in density-stratified fluids. *J. Fluid Mech.,* **289,** 115–128.
Winton, M., R. Hallberg, and A. Gnanadesikan, 1998: Simulation of density-driven frictional downslope flow in *z*-coordinate ocean models. *J. Phys. Oceanogr.,* **28,** 2163–2174.
Wood, I. R., 1965: Studies of unsteady self preserving turbulent flows. Australian Water Research Laboratory Rep. 81, University of New South Wales, Sydney, NSW, Australia.

Unauthenticated | Downloaded 12/09/24 12:22 AM UTC